FY21 Joint Research Target: Shattered Pellet Injection for Disruption Mitigation on ITER Q4 Progress Report

Prepared by:

D. Shiraki[1], N. Eidietis[2], E. Hollmann[3], S. Jardin[4], R. Sweeney[5]

With contributions from:

D. Bonfiglio[6], R. Granetz[5], J. Herfindal[1], V. Izzo[7], C. Kim[8], J. Kim[9], B. Lyons[2], A. Matsuyama[10], J. McCleneghan[2], C. Paz-Soldan[11], U. Sheikh[12], B. Stein-Lubrano[5]

[1] Oak Ridge National Laboratory, Oak Ridge, TN
[2] General Atomics, San Diego, CA
[3] University of California - San Diego, La Jolla, CA
[4] Princeton Plasma Physics Laboratory, Princeton, NJ
[5] Massachusetts Institute of Technology, Cambridge, MA
[6] Consorzio RFX, Padua, Italy
[7] Fiat Lux, San Diego, CA
[8] SLS2 Consulting, San Diego, CA
[9] Korea Institute of Fusion Energy, Daejeon, Republic of Korea
[10] National Institutes for Quantum and Radiological Science and Technology, Chiba-shi, Japan
[11] Columbia University, New York, NY
[12] École Polytechnique Fédérale de Lausanne, Lausanne, Switzerland

Table of Contents

Statement of Annual Joint Research Target:

Conduct research to assess the capability of the shattered pellet injection (SPI) system for use as the ITER baseline disruption mitigation system technology. Coordinated multi-institutional research will explore the capability of SPI to radiate the plasma thermal energy and control current quench characteristics while at the same time providing high plasma densities for runaway electron suppression through the superposition of multiple SPI, as is envisioned for ITER. The research will utilize existing SPI systems on DIII-D and JET, and possibly data from a planned system on KSTAR as well, and make comparisons with computational studies utilizing extended MHD codes. Additional activity would include evaluation of potential alternative injection and mitigation techniques.

Statement of 4th Quarter Milestone:

Complete the required analysis of experimental and computational results. Prepare a joint report summarizing the findings of the JRT research, including identification of established areas of consensus and remaining questions for extrapolating SPI performance to ITER.

The 4th Quarter Milestone has been completed with the preparation of the final JRT report, which follows. This report summarizes both the additional analysis completed in the final quarter, along with the progress and results previously described in the Q1-Q3 reports. An executive summary of findings, followed by details of the research, are given.

Executive Summary

The 2021 Joint Research Target (JRT) collected input from the DIII-D, JET, and KSTAR tokamaks, to help assess the ability of SPI to fulfill the requirements of the ITER Disruption Mitigation System (DMS). The collective results from recent experiments through collaborations at the three facilities have provided data covering a range of device size and parameter regimes, injector distributions, and diagnostic configurations. In addition, dedicated DIII-D experiments were planned and executed in support of this JRT activity. Experimental results from the three facilities have also been compared with associated modeling, utilizing both extensive deployment of reduced models as well as select cases using leadership-class simulations. This report summarizes current progress on this topic based on the collective findings of these experimental and modeling activities.

Good progress was made in identifying several areas where the results from multiple facilities support a consistent picture of the physics basis for SPI performance:

- *The global dynamics of high-Z SPI are largely determined by volume-averaged energy balance.* Data from all three tokamaks are accurately reproduced by 0D KPRAD simulations that consider only the time-dependent global energy balance of the plasma-SPI interaction. This experimentally validated model provides predictive capabilities applicable to ITER, and additionally provides a tool for guiding more-accurate but less-versatile 3D extended MHD codes (e.g. in large parameter scans). Limitations are primarily encountered when the fraction of high-Z impurity in the species mixture is low.

- *Thermal quench (TQ) radiation asymmetries due to high-Z impurity radiation from SPI are close to estimated allowable values for the ITER wall.* The localized nature of the impurity source contributes significantly to this peaking, but the asymmetry due to n=1 MHD modes may also contribute. It is not yet fully demonstrated that spatially distributing the particles across multiple injectors reduces this peaking, although preliminary results suggest this may be the case given synchronization within the pre-TQ timescale.

- *The assimilation of hydrogenic pellets by the thermal plasma is found to be limited, with typical injection quantities used in current studies leading to a delayed disruption determined by subsequent MHD growth.* Assimilation is thought to be limited by radial particle transport. Further density increase through additional pellets with good synchronization appears to be viable, but still requires further study.

- *Access to global MHD instabilities in mature runaway electron (RE) beams with a recombined background enables benign termination of the beam.* Hydrogenic SPI into fully formed RE beams is found to recombine the background plasma, above a critical injected quantity. When a global MHD stability boundary is crossed in this plasma state,

rapid and broad MHD-driven dispersal of the REs is observed in both DIII-D and JET. The phenomenology and access conditions for this type of loss event are described.

In addition to the above areas of growing consensus, further details of analysis from the three individual facilities, including areas that have not necessarily been studied on the other devices, are given in the subsequent Section of the report. These descriptions supplement the above discussions of the areas of common findings, and summarize and expand on the progress described in the Q1-Q3 reports.

Although the areas listed above have demonstrated improved understanding, several significant questions remain for the extrapolation of SPI performance to ITER. Areas warranting further study in the near future include: effects of distributing the particle source over multiple injectors, predictive understanding of radial particle transport limiting low-Z SPI assimilation, ideal distributions of fragment sizes within the shatter plume, the propensity for RE seed formation during the SPI TQ, and detailed understanding of the relatively new approach for RE mitigation based on benign termination. Discussions of these topics, current levels of understanding, and suggestions for future research in these areas are given.

Because of the significant challenges for disruption mitigation in ITER, potential alternative injection techniques that could be considered for subsequent DMSs, are also discussed. These techniques have been studied due to possible relative advantages compared to SPI, which are described, but currently have limited technical demonstrations of their capabilities.

Archived data from Alcator C-Mod were also analyzed for the JRT, in order to compare the effects of disruptions due to unplanned impurity influx from the wall (so-called "UFOs") with those of intentional triggering of the DMS. Since C-Mod was not equipped with an SPI system, comparisons were made with massive gas injection (MGI) shutdowns. While these UFO influx events have some similarities to DMS shutdowns, these results demonstrate the incomplete nature of the resulting "mitigation", and further emphasize the need for a comprehensive disruption prediction, avoidance, and mitigation approach, of which SPI (or other DMS) is just one component.

Overall, the JRT activities have provided opportunities for good cross-machine comparative studies, and strengthen the available physics basis for SPI. Continued collective efforts through other available avenues (e.g. the ITER Disruption Task Force, or International Tokamak Physics Activities) are essential for continued progress.

The results described in this report are provisional, and are subject to further revisions.

1. Introduction

The ITER Disruption Mitigation System (DMS) will use shattered pellet injection (SPI) as the primary technology in its baseline design [Luce2021], utilizing large cryogenic pellets to rapidly deliver large particle quantities while maximizing the assimilation of this material by intentionally shattering the pellets just prior to their entry in the plasma [Combs2010]. In order to deliver the required large material quantities and to minimize asymmetries, the shattered pellet material will be input from a distributed set of injectors across several ITER port plugs.

The ITER DMS is essential for successful execution of the ITER Research Plan [ITER2018], and is tasked with the specific goals to:
- Mitigate melting and erosion of plasma-facing components due to thermal loads
- Maintain CQ rates within allowable ranges, in order to mitigate electromagnetic loads due to halo and eddy currents
- Suppress the formation of, or mitigate the damage from, runaway electrons (REs).

These are a challenging set of requirements due to the large stored thermal and magnetic energies in ITER plasmas, necessitating a high level of particle assimilation for both thermal mitigation and RE suppression/dissipation. Simultaneously, CQ times must remain within a finite window in order to avoid the opposing limits for halo and eddy currents. Additional constraints are introduced by limits on allowable injection quantities, due to impacts on pulse rate (which becomes limited by vacuum vessel pump-out and loading of the gas-handling systems) as well as possible effects on performance of the subsequent pulse [ITER2018]. Ensuring these criteria are met requires a sound physics basis for understanding the SPI performance.

The effectiveness of the ITER DMS will depend on a number of key parameters of the injected materials. For the SPI method of particle delivery, a number of parameters must be optimized: the distribution of fragment sizes within the shatter plume; quantity and composition of injection species (hydrogen, neon, and/or their mixtures); and the sequence of the various species and pellets to be injected. Some of these parameters will be determined once the design of the DMS hardware is finalized, based on the shatter tube impact angles and pellet size/speed (as determined by barrel size, propellant pressure, the use of mechanical punches, etc.). However, beyond these design choices, the performance of the system can be further tuned based on the species mixtures and their sequence of delivery. Some examples of possible injection schemes include: 1) an initial low-Z (hydrogenic) injection to cool the plasma without inducing a thermal quench (TQ), with a subsequent high-Z (neon) or mixed-species injection to enhance radiation; 2) initial high-Z injection to maximize radiation with rapid response, followed by hydrogenic injection to dissipate REs; or 3) simultaneous delivery of low- and high-Z materials via synchronous mixed-species injection. Such operational choices will also be made based on the plasma state when the DMS is triggered, in order to optimize performance for a given scenario. In order to finalize these design choices and effectively guide its operations, a validated physics

basis for predicting the resulting mitigation performance as a function of the available knobs, is needed.

This effort to establish a mature physics basis for the ITER DMS continues to be an active field. The first SPI studies were carried out on DIII-D and showed promising results [Commaux2010, Commaux2011, Commaux2016, Shiraki2016], particularly in terms of how the technique compared to equivalent massive gas injection (MGI), which at the time was being considered as a technology for the ITER DMS. This led to a full adoption of SPI over MGI for the ITER DMS following a 2017 review. Since this decision, SPI research to guide the ITER DMS design has also expanded internationally to several additional tokamaks. Currently, the US is collaborating on the SPI projects at JET and KSTAR, through development of the injector systems and participation in the scientific programs. In addition, the DIII-D program continues to invest heavily in its SPI studies in support of ITER. The JRT activities incorporate results and findings from these three programs, to better identify the common understandings and remaining gaps for the ITER SPI design basis.

Each of these three facilities offers unique capabilities and available datasets, and the more notable features and contributions from each are listed here (note this is not a full list of relevant diagnostics and capabilities):

- DIII-D is equipped with two SPIs, located above the midplane and distributed 120° apart toroidally. CQ density measurements are available, based on interferometry and Thomson scattering. RE beam formation from high-Z killer pellets or MGI is routinely available. DIII-D also possesses a large historical database of SPI shots dating to 2009.
- JET possesses the highest plasma currents and stored kinetic energy within the group, with ITER-like wall materials. A single SPI from an upper port is installed. RE beam formation from MGI is available.
- KSTAR is equipped with two SPIs, matching the ITER geometry with midplane injectors distributed 180° apart toroidally. CQ density measurements are possible with a new dispersion interferometer. Several new SPI-specific diagnostics have been installed along with the injectors, and are being commissioned.

Collectively, the set of three facilities offers a wide ranging parameter space and suite of measurement capabilities. This report describes progress based on results from across these collaborations, identifying areas of progress and remaining gaps.

Some of the results described in this report have been recently published, and a list of these works are given at the end of the report. See "Recent Publications from DIII-D, JET, and KSTAR SPI Research (FY 2021)".

2. Areas of common findings across facilities

The recent deployment of SPI on JET and KSTAR have significantly expanded available data, and notably makes possible the comparison of findings and observations across the three facilities. Although the experimental selections for each research program were conducted independently from each other, the combined datasets from the various facilities have identified several areas of emerging consensus on the physics basis determining SPI performance. Here, specific areas of agreement are described.

2.1 Global dynamics of high-Z SPI

When neon is a primary injection species, impurity radiation becomes the dominant factor in determining the disruption dynamics. The 0D KPRAD code [Whyte2003,Hollmann2008] with a modified SPI ablation particle source [Parks2017], has been extensively applied to model experiments from all three facilities, and are successful in reproducing observations based on this picture. This reduced model tracks the shielding-limited ablation of individual SPI fragments, the subsequent evolution of all charge states for the impurity and fuel species as the ablatant is ionized, and the resulting plasma evolution. While 3D effects (such as MHD mode growth, or the localized nature of the injection source) are always present, certain globally averaged parameters of the disruption can be accurately predicted without consideration of these factors.

The wide applicability of this model can be seen in Figure 2.1.1, which compares the KPRAD calculation of the CQ rate to experimental data spanning DIII-D, JET, and KSTAR. The agreement is excellent over an order of magnitude in values, with the exception of a small number of low-energy JET discharges (W_{th} < 0.8 MJ) where the particularly low assimilation rates are difficult to model precisely.

The resulting SPI particle assimilation and CQ density rise in the KPRAD model have been compared with the available measurements from DIII-D and KSTAR, as shown in Figure 2.1.2. A small number of KSTAR neon SPI discharges with available interferometry (left) and DIII-D shots that cover a wide range of plasma thermal energy spanning nearly a factor of 10 (right) are compared and show excellent agreement. Thus assimilation of neon SPI is limited by the thermal energy available for ablation, with no evidence of additional processes (e.g. transport) that would significantly reduce this assimilation fraction.
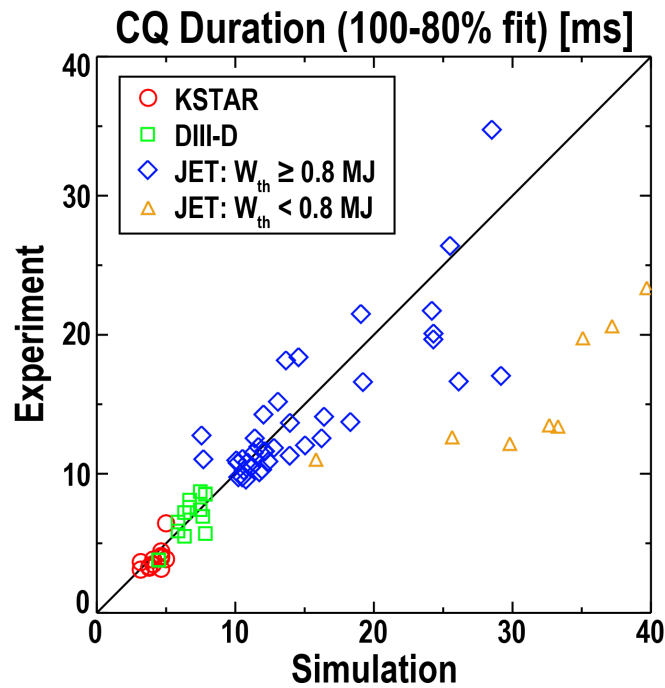
Figure 2.1.1: *Comparison of experimental CQ duration to KPRAD model for DIII-D, JET, and KSTAR SPI data.* Good agreement is found spanning an order of magnitude across the three devices.
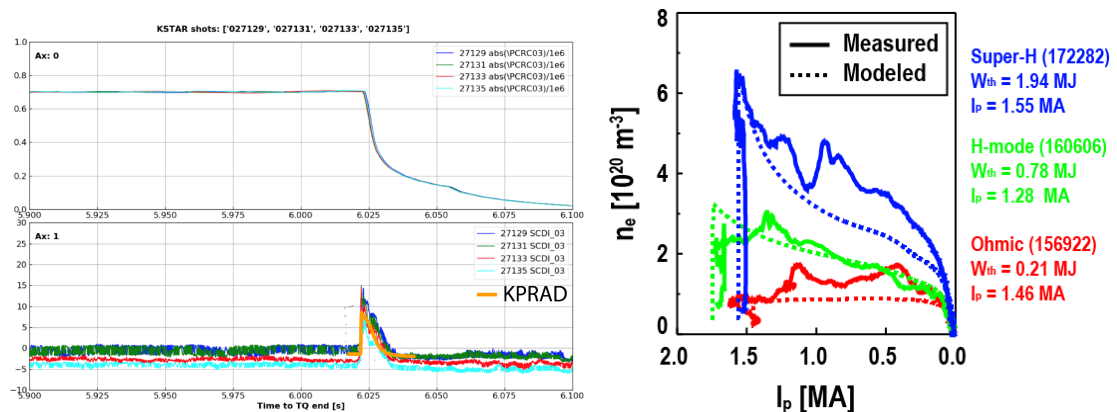

Figure 2.1.2: *Comparison of measured and simulated density perturbations during the neon SPI CQ, on KSTAR (left) and DIII-D (right). The DIII-D discharges span nearly a factor of 10 in stored energy.*

Another important parameter captured by KPRAD is the cooling time following SPI, which is given by the time delay from the pellet arrival at the plasma edge to the current spike at the start of the CQ, equivalent to the duration of the pre-TQ and TQ processes. This comparison, as a function of neon quantity within the injected pellets in JET and DIII-D, are shown in Figure 2.1.3. Prediction of the cooling time is especially important, as it determines how long solid fragments

can be effectively ablated and assimilated prior to the dropping electron temperature leading to significant slowing of these processes.
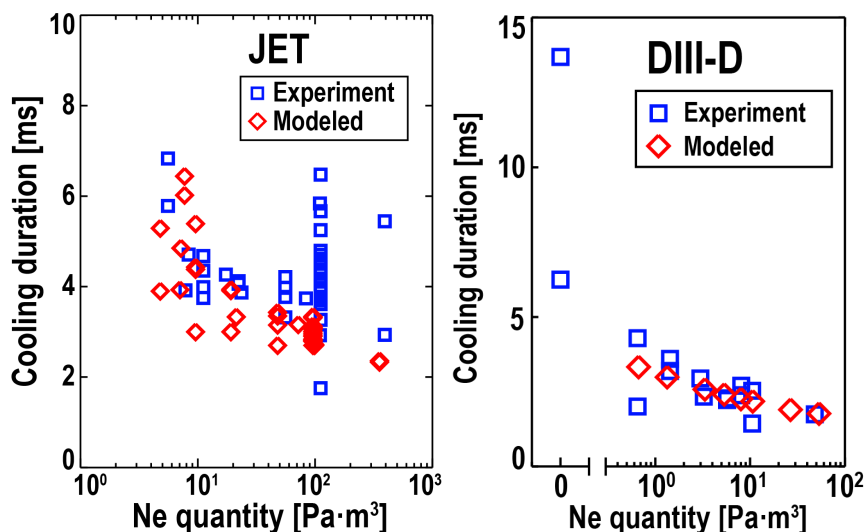

Figure 2.1.3: *Comparison of measured (red) and KPRAD-modeled (blue) cooling durations during SPI injection of varying Ne quantity in JET (left) and DIII-D (right).*

Thus overall, the extensive comparisons of KPRAD with DIII-D, JET, and KSTAR results give confidence in its applicability to predicting certain global metrics for ITER SPI shutdowns with significant radiating impurities. The reduced model is also significantly faster than full 3D MHD codes, and allow rapid parameter scans that can guide not only future experimental efforts but also for th planning of large leadership-class simulations.

The KPRAD model does run into limitations in certain regimes, when the injected species is either purely or dominantly deuterium. In these discharges, the neon radiation plays a less dominant role in the shutdown dynamics. Since this is the primary physics tracked by KPRAD, it's applicability declines. Other physics mechanisms not included in KPRAD become more important (as discussed further in the report). This distinct transition (when neon is eliminated) can be seen in Figure 2.1.3 (right), where the neon-free pellets exhibit a sudden transition and significant spread relative to the well-predicted trend for pellets containing neon.

Additional points should be noted in the application of KPRAD simulations to the prediction of future ITER discharges. The CQ characteristic that KPRAD accurately predicts (and which is shown in Figure 2.1.1) is the *initial* CQ rate, given here based on the 100-80% portion of the CQ. This quantity can be accurately modeled because this initial decay rate is largely a function of the plasma resistivity and is thus determined by the TQ neon assimilation. In contrast, details of the subsequent evolution (e.g. the CQ characterized by the 80-20% metric used by ITER) are dependent on additional details such as the plasma's vertical displacement during the CQ, and thus are not accurately reproduced by KPRAD. Coupling of KPRAD predictions of the initial CQ

rate (and plasma temperature) with geometrically resolved CQ evolution simulations (such as DINA) would provide more accurate predictions.

2.2 Radiation asymmetry

Even assuming full radiation of the thermal energy, localized melting can still occur in ITER if the radiation intensity is too high in places. Quantitative estimates of this peaking (for single-injection neon SPI) have been derived on DIII-D and JET, based on several independent experimental and simulation-based approaches. These various methodologies independently arrive at toroidal peaking factors (TPFs) in the range of 1.7 to 2.5. These values span the estimated value of 2.0 at which the highest energy ITER plasmas could cause localized melting [Sugihara2007]. The various approaches and resulting estimates are presented in this section concluding with a summary table.

In DIII-D, the dual injectors are used in repeat discharges with identical pellets to observe the changes in wall heating using the wide-angle periscope-view IR camera. The cooling of the tiles is observed after the disruption and mapped back to the time of the TQ using a model for the tile surface temperature evolution [Hollmann2015]. Differencing the observed heating between two discharges with toroidally displaced injections and fitting a helical radiation feature with a Gaussian falloff, a TPF is derived. This method is benchmarked on MGI discharges and finds a TPF of 1.3 +/- 0.1, which is in good agreement with previous radiometer based estimates [Shiraki2015]. When applied to single-injection neon SPI discharges, the TQ TPF is estimated to be 1.9 +0.5/-0.3. Figure 2.2.1 shows the fitted distributions separated into TQ and CQ contributions (left) and the resulting TQ TPF as a function of the assumptions on the TQ and CQ radiated fractions (middle).
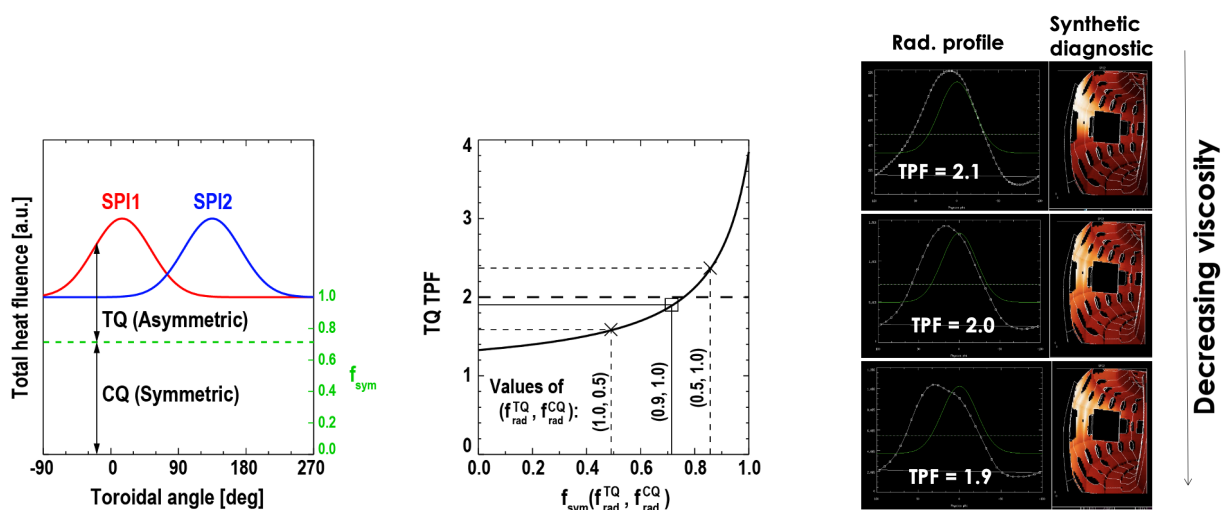

Figure 2.2.1: *Thermal quench TPF at DIII-D following single pellet injection, from experimental analysis (left and center), and from NIMROD simulations (right).*

The NIMROD 3D MHD code is used to simulate these DIII-D single SPI discharges [Kim2021], where TPFs are straightforwardly computed from the simulated plasma emissivity (Figure 2.2.1 right). The viscosity has been scanned across simulations to affect the MHD evolution, and only a modest change is found within the range simulated, with slightly lower TPFs found for lower viscosities. In both the experimental IR data and NIMROD simulations, the radiation peak is broadly centered around the SPI port, indicating that the localized impurity source is a primary driver of the radiation asymmetry.

At JET, an experiment campaign (M18-34) investigated the radiation asymmetries during SPI shutdowns by varying the toroidal phase of an applied n=1 field. In the discharges shown in Figure 2.2.2, the n=1 field is energized during a stable H-mode flattop, with the SPI fired shortly afterwards. The toroidal phase of the n=1 field is varied shot-to-shot and the radiation is measured using two bolometer fan arrays displaced from the injection by 90° and -135° degrees (the vertical V and horizontal H arrays, respectively). The time of peak radiated power is used to determine the TPF. A sinusoidal distribution is assumed for the radiation with fit parameters Δp and $\Delta\phi_{n=1}$ to adjust the amplitude of the asymmetry and the relative phase of the asymmetry to the locked mode O-point. A Gaussian distribution is used to describe the toroidal spread of impurities about the injection and λ_ϕ is a fit parameter allowing variation of the spread.

$$p_{dis}(\phi) = 1 + \Delta p \cos(\phi_{n=1} - \Delta\phi_{n=1} - \phi)$$
$$n_i(\phi) = n_{i,0} \exp\left(-(\phi - \phi_{inj})/\lambda_\phi^2\right)$$

The product of the cosine and Gaussian distributions and the average radiated power then give the toroidally resolved radiated power.

$$P_{rad}(\phi) = \langle P_{rad}(\phi) \rangle \, p_{dis}(\phi) \, n_i(\phi)$$

Finally, the TPF is found using the P$_{rad}$ distribution as follows:

$$TPF(\phi_m) = P_{rad,max}(\phi_m)/\langle P_{rad}(\phi_m) \rangle$$

The asymmetry factor derived from the vertical (V) and horizontal (H) bolometer arrays is shown in Figure 2.2.2 (left) and the resulting TPF as a function of the locked mode phase in Figure 2.2.2 (right). The toroidal peaking is found to depend on the toroidal phase of the locked mode, reaching a maximum of 1.7 when the O-point is approximately aligned with the injection. This suggests that the asymmetric MHD heat flux due to the n=1 mode may also play a role in driving the radiation asymmetry, in addition to the localized impurity source identified here and in the DIII-D results.
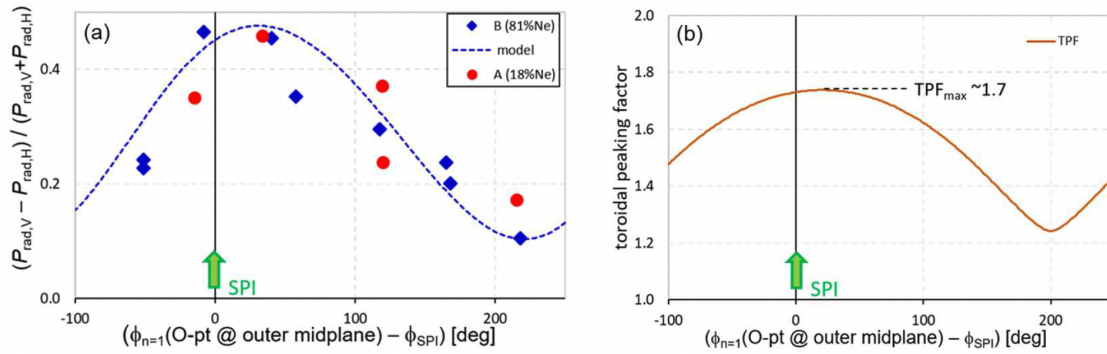
Figure 5: (a) Radiation asymmetry factor taken at the time of the maximum P_{rad}-peak as a function of the toroidal n=1 O-point location with respect to the SPI location for two data sets using different pellet types. The dashed line corresponds to the model fit using the data from the pellet B data set only. The fit parameters are $\lambda_n=135^o$, $\triangle p=0.22$, $\triangle \phi_{n=1}=-20^o$. (b) Resulting toroidal peaking factor as function of n=1 O-point location.

Figure 2.2.2: *Radiation peaking is determined on JET by scanning the phasing of an applied n=1 field. Figure and caption from [Jachmich2021].*

A second approach is used on a different SPI experiment campaign on JET (M18-32), which yields higher TPF estimates. Approximately 110 helical (field aligned) radiation distributions are sampled by synthetic horizontal and vertical bolometer arrays using the Cherab ray-tracing code, which then provides diagnostic responses for each of these distributions. These response vectors are then independently fit at each bolometer sample time and the helical distribution with the lowest reduced chi-squared is chosen. With this helical distribution, a Gaussian toroidal distribution can be superimposed and constrained by the measurements at the two bolometer arrays. This radiation distribution is then used to infer the instantaneous P_{rad} and TPF. The full disruption integrated radiated fraction is shown in Figure 2.2.3 (top) and the TPF at the maximum in P_{rad} in Figure 2.2.3 (middle). The TPFs estimated based on this technique are slightly higher than the previously described approaches, being in the range of 2.2 +/- 0.2.
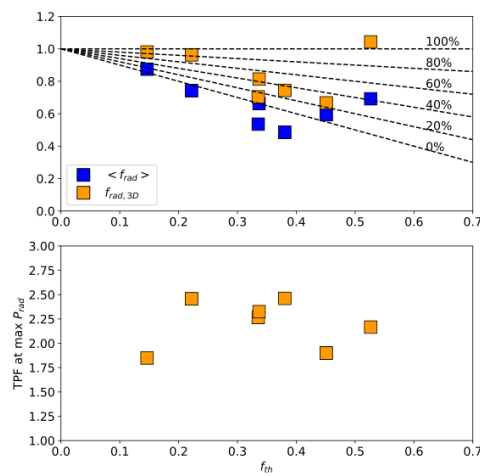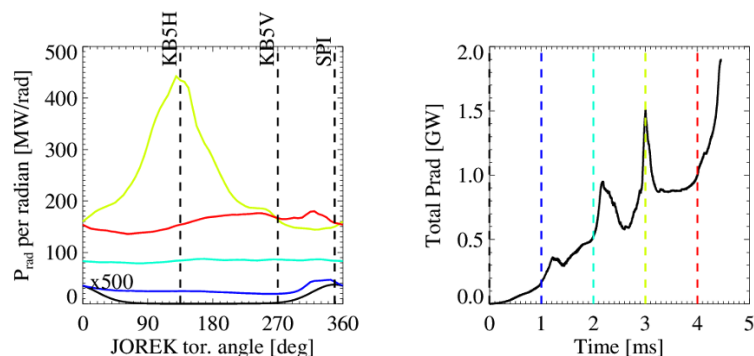
Figure 2.2.3: *(Top) Full disruption radiated fraction and (middle) the TPF at the time of the maximum in Prad, from [Sweeney2020].* (Bottom) shows JOREK radiation profiles and total power evolution.

JOREK simulations [Bonfiglio2020] have been applied to discharges from the same JET experiment campaign as those reported in [Sweeney2020] but with higher current and thermal energy. The toroidal radiation distribution at the time of peak radiation is shown in yellow in Figure 2.2.3 (bottom-left). Note that the peaking is localized in time as shown by the time-trace of P_{rad} in Figure 2.2.3 (bottom-right). Interestingly, the toroidal peak is located almost opposite the injector, which is indicated by the vertical-dashed line in the bottom-left (labeled "SPI"). This has also been observed in simulations of MGI [Izzo2015] and in some DIII-D SPI experiments [Sweeney2021], though it has not yet been observed in the SPI experiment campaign on JET; further experimental analysis will look for instances of this.

The above TPFs are estimated for a single injection location, and an important question is whether injection from multiple locations is able to lower the peak heat loads through a broader impurity distribution. This has not yet been conclusively demonstrated, but preliminary experimental results from DIII-D and ITER simulations suggest this is the case. In DIII-D, toroidally displaced AXUV array measurements of radiated power during dual-SPI experiments are consistent with lower radiation near the original peaks and enhanced radiation at more distant locations, qualitatively consistent with a broader more uniform distribution. Toroidal resolution of the available data is rather coarse, however. Simulations of two diametrically opposite SPIs in ITER suggest that the toroidal peaking might be significantly reduced compared to a single SPI [Hu2021]. At the time of peak radiation shown in red in Figure 2.2.4 (right) the maximum toroidal asymmetry is ~1.3 as shown in red on the left. These simulations are encouraging and motivate further experimental studies.

The technical requirements for such broadening through multiple injections require synchronization of the multiple pellets within the timescales the cooling duration timescale. This is consistent with the results of the timing scan in similar dual-SPI results published in [Herfindal2019].
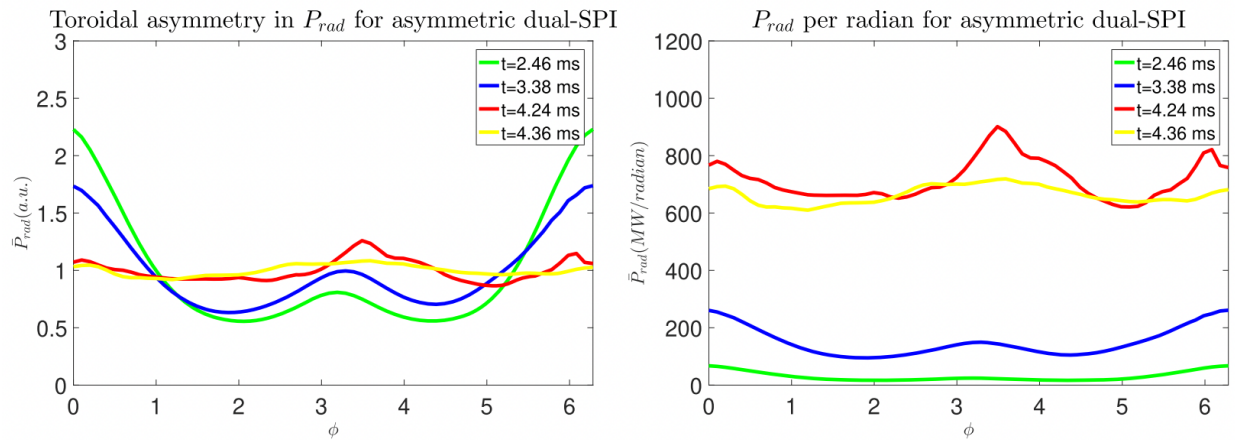
Figure 2.2.4: *Dual SPI into an ITER discharge. (left) spatial resolved toroidal peaking (i.e. $P_{rad}(\phi)/<P_{rad}>$) at four time slices and (right) the total radiated power.*

Table 1 below summarizes the present state of toroidal asymmetry measurements following SPI.

Device	Technique	Toroidal distribution	Time of measure	TPF
DIII-D [Shiraki2020]	IR periscope, difference of two shots, helical	Gaussian	TQ integrated TPF	1.9+0.5/-0.3
DIII-D [Shiraki2020]	NIMROD - single injection	--	At max Prad	1.9-2.1
JET [Jachmich2021]	Applied n=1 field, ring source	Cosine*Gaussian	At max Prad	1.7
JET [Sweeney2020]	Emis3D - helical, ray-tracing	Gaussian	At max Prad	2.2 +/- 0.2
JET [Bonfiglio2020]	JOREK - single injection	--	At max Prad	1.8
ITER [Hu2021]	JOREK - single injection	--	At max Prad	2.5
ITER [Hu2021]	JOREK - dual injection	--	At max Prad	1.3

Table 1: *Summary of the toroidal peaking measurements and simulations following SPI.*

2.3 Assimilation of hydrogenic pellets prior to the TQ

It is observed in all three devices that injection of pure deuterium SPI, at the typical quantities used in these studies, is often insufficient for immediately triggering a disruption. Examples of this delayed response are shown in Figure 2.3.1 for DIII-D (7 mm pellets) and JET (12.5 mm pellets), where the timescales of up to 10's of ms before the CQ start can be contrasted with the significantly faster timescales during similar neon-SPI, as shown in Figure 2.1.3. (The DIII-D data in particular include the pure deuterium pellets, and clearly show the discontinuity in timescales when no neon is included in the pellet.)
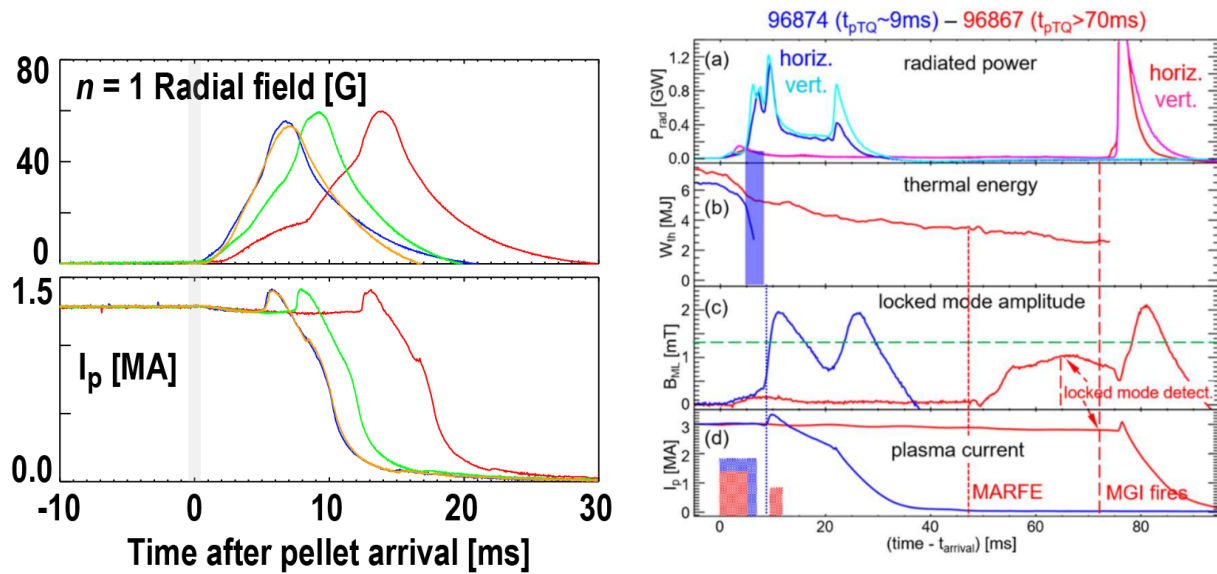

Figure 2.3.1: *TQ following D2 SPI occurs after n=1 mode grows to critical amplitude, on DIII-D and JET.*

The importance of n=1 MHD growth in setting this timescale can be seen in Figure 2.3.1, showing the significantly different mode evolutions than can be observed under repeat conditions, and their correlation between this growth and the delay in CQ-onset.

The mechanism for this mode growth to lead to a TQ is thought to be identical to a locked mode disruption. This relationship is supported by data from all three machines, where an empirical scaling for the locked-mode threshold [deVries2016] matches that measured by saddle loops on all three machines, as shown in Figure 2.3.2. However, KSTAR is not especially sensitive to this measurement due to the large distance between plasma and saddle loops, resulting in the small signal levels seen in the Figure.
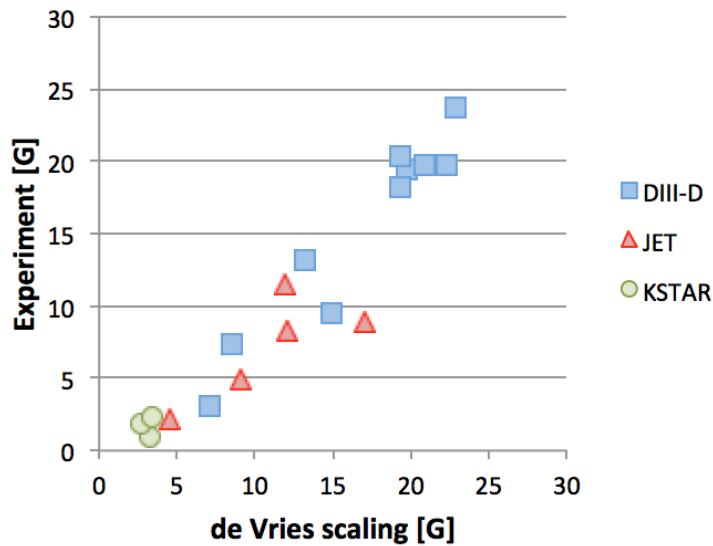
Figure 2.3.2: *Comparison of experiment n=1 MHD amplitude at time of disruption following D_2 SPI to deVries scaling. From [Shiraki2021].*

As has been noted earlier, the KPRAD model diverges from experimental observations when the shutdown is by D_2 SPI, with the absence of any high-Z radiator. More specifically, this is generally the case for small and medium D_2 SPI (< ~7mm on DIII-D), but extremely large amounts of D_2 SPI (e.g. 16mm pellet on DIII-D) are capable of cooling the plasma to such an extent that a CQ is directly initiated, and this evolution is relatively well-captured by KPRAD. For the cases of more modest sizes of D_2 SPI, the important mechanism of n=1 MHD mode growth (as opposed to radiative cooling) is not included in the physics modeled by KPRAD.

In such cases, the 1D INDEX code [Matsuyama2021] is being used to understand this radial transport effect. Post-SPI profile measurements on DIII-D provide a test bed for such simulations, as will be described in Section 4.

2.4 Effect of hydrogenic pellets on runaway beam

DIII-D and JET find common observations of mature RE beam benign termination when a global MHD stability boundary is crossed after injection of deuterium SPI. Note that since RE beams are not routinely formed on KSTAR, this study remains to be performed there. Detailed description of the results can be found in [Reux2021,Paz-Soldan2021], with a summary given here. As compared to the baseline approach of high-Z collisional dissipation, which is predicted to result in only modest heat load reduction, these findings present a novel approach to mature RE beam mitigation for ITER.
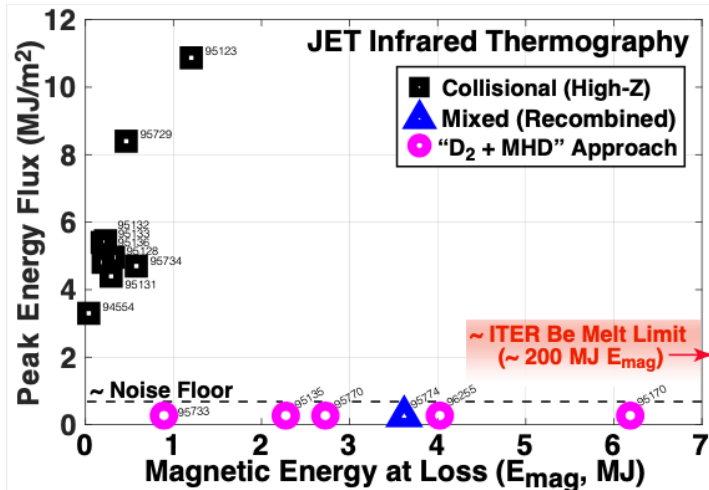
Figure 2.4.1: *Peak energy fluxes as measured by IR thermography on JET indicate an absence of measurable heating despite large stored magnetic energy in the RE beam for the D2+MHD approach, in contrast to the collisional approach.*

The basic features are the same on both DIII-D and JET. First, REs are intentionally created for study using Ar primary injection to trigger the RE-producing disruption. Shortly following the disruption, secondary D_2 injection immediately recombines the background plasma due to an enhancement of the neutral heat conduction with D_2 that drops in bulk T_e below the ionization threshold [Hollmann2020]. The recombined background plasma yields a relatively collisionless RE beam state, which due to the very low density possesses an exceptionally fast Alfven speed, comparable to the speed of light. If a global MHD limit is crossed, for example at low edge safety factor (q_a), or with a sufficiently hollow current profile, extremely large and fast MHD instability is accessed. The MHD then effectively causes a second disruption of the RE beam, often complete with an I_P-spike. During this event the REs are found to be completely expelled over a large wetted area, minimizing localized heating. Furthermore, since so few REs survive the disruption, the conventional process of re-avalanching is dramatically reduced, and the current transfers directly to the bulk. This effect prevents the transfer of magnetic energy to damaging RE kinetic energy. Instead, the magnetic energy dissipates as line radiation during the now conventional Ohmic CQ. While the basic features are the same, differences in the critical q_a are found. DIII-D finds instability at conventionally low values (q_a ~ 2 or 3), while JET finds instability at higher values (q_a ~ 3 - 5). This is interpreted as being due to a broader (or hollow) current profile on JET as compared to DIII-D, and the possibility of tearing modes playing a larger role in the MHD events [Bandaru2021].

The benign termination scenario is being both further exported to other tokamaks worldwide as well as being studied for extrapolation to ITER. In ITER, the vertically unstable equilibrium during the CQ is expected to cross low-order edge safety factor rationals, indicating the potential for the same large-scale MHD. The possibility of recombining the background plasma in ITER is being studied, with an important difference being the use of neon and hydrogen in

ITER (instead of argon and deuterium in present devices). RE orbit loss modeling is being used to quantify the degree of heat flux spreading expected as a function of instability size. Finally, due to the large avalanche gain in ITER, it is possible that multiple benign termination events will be needed to mitigate a full current ITER RE beam.

3. Highlighted results from individual facilities

The previous Section describes areas of emerging agreement, with consistent observations and interpretation arising from multiple machines. Additional analysis and results from research on individual facilities activities are described here.

3.1 DIII-D

In 2021, a dedicated DIII-D experiment (MP2019-25-15) was executed in support of this JRT, with the equivalent of two rundays aiming to investigate the assimilation limits for deuterium SPI. This experiment added to the large body of existing D_2 SPI experiments [Commaux2010,Commaux2011], with the addition of two new SPI barrel sizes (or equivalently injection quantity) and several new diagnostic capabilities now available. The new diagnostic capabilities include significant improvements to Thomson scattering (TS) profile measurements, which now include both low-temperature polychromators allowing measurements of just a few eV throughout the core region, as well as asynchronous (pellet light) triggering of the TS for systematic measurements of the post-SPI profiles. Additionally, particle flux measurements using particle probes are newly available on DIII-D; these data were previously unavailable due to administrative limits.

In contrast to high-Z SPI shutdowns in which impurity radiation plays a dominant role, other physics mechanisms (e.g. MHD growth, radial transport, and intrinsic impurities) are thought to become important. Assimilation of D_2 SPI injected material is important for heat load reduction, current decay rate, and runaway electron suppression. Previous experiments on DIII-D have demonstrated that SPI assimilation tends to be better than MGI assimilation. However, even for SPI, the assimilation is far below 100%. Figure 3.1.1 shows an example of D_2 SPI assimilation for a variety of different injected quantities, with roughly similar target plasmas. The assimilation is estimated from line-integrated CO_2 interferometers, assuming 100% ionization fraction in the plasma, and neglecting impurities. The middle of the CQ is used here, since toroidal asymmetries are believed to be large during the TQ and vertical drift makes electron density measurements harder to interpret past the middle of the CQ. Overall, it can be seen that the mid-CQ assimilation appears to be well below 50%, perhaps more typically around 20 – 30%.
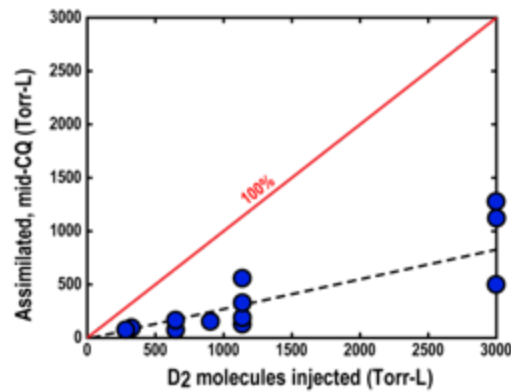
Figure 3.1.1: *Mid-CQ assimilated D_2 quantity as a function of injected quantity for different shots.*

Alternate measurements confirm the number of particles injected, providing confidence that the assimilation fraction is not mis-estimated due to inaccurate pellet sizing. This can be seen from the post-disruption pump-down of the vessel, when pressure readings vs time can be used to estimate the amount of particles pumped out of the vacuum vessel. Figure 3.1.2 shows estimates of the amount of D_2 pumped out of the vessel post-disruption compared with the claimed amount injected. Although the scatter in the data is quite large, it does appear that the amount of D_2 recovered is consistent with the amount injected. This suggests that (a) the injected quantity is correct, and (b) the amount of wall absorption/release during the shutdowns is not dominant compared with the amount injected. This is reasonable, since typical wall release during disruptions is of order the plasma particle inventory (~20 Torr-L D_2), which is small compared with the injected quantity (~500 Torr-L D_2).
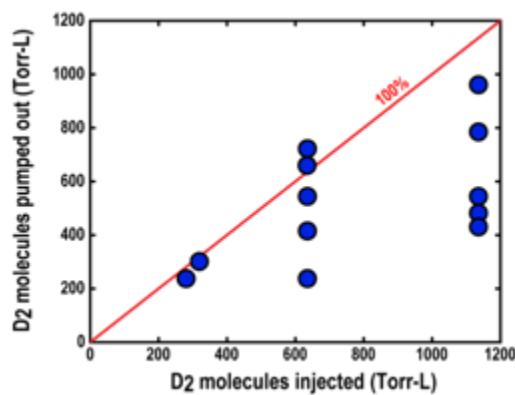

Figure 3.1.2: *Amount of D_2 recovered post-shutdown by the DIII-D pumping system, compared with the amount injected.*

Figure 3.1.3 shows an example of total free electron number vs time in the plasma estimated assuming toroidal symmetry using (red) TS at toroidal angle = 150° (close to the SPI injection location of = 135°) or CO_2 interferometer at toroidal angle = 225° (far from the SPI injection location). It can be seen that there appears to be some disagreement, perhaps 50% at the peak

density, but not the factor of 4 seen in Figure 3.1.1. Based on this preliminary comparison, we therefore conclude that some of the missing mid-CQ particles could arise from toroidal asymmetries, but probably not the full factor 4.
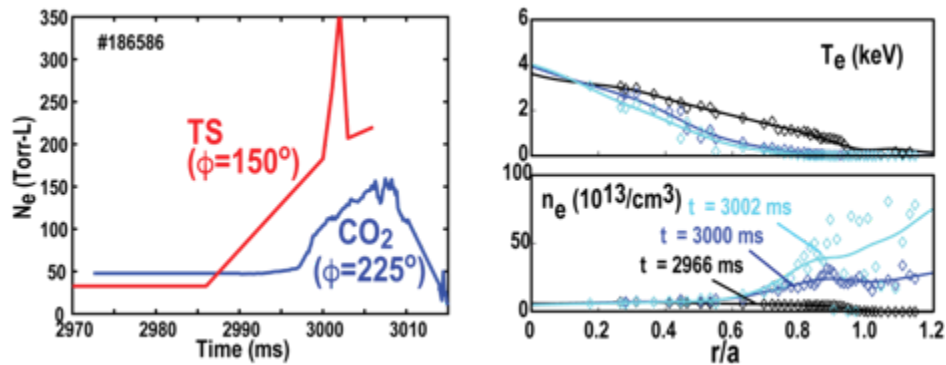

Figure 3.1.3: *Comparison of (left) total electron number from TS vs CO2 interferometers, and (right) examples of TS profiles of Te and ne during SPI shutdown.*

A single-point measurement of main chamber particle flux was obtained in 2021 using the midplane plunging probe. For these experiments, the probe was not plunged, but was left fixed near the main chamber wall to measure ions hitting the wall. Figure 3.1.4 gives an overview of time traces during a D_2 SPI shutdown. It can be seen that there is main chamber plasma flux during all stages of the shutdown, during the TQ, the I_p spike, and during the CQ. Wall flux typically appears to be largest during the I_p spike.
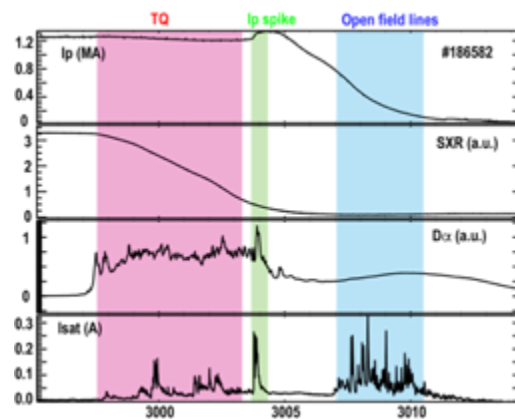

Figure 3.1.4: *Time traces of a D_2 SPI shutdown showing (a) plasma current, (b) central soft x-ray brightness, (c) D brightness, and (c) midplane probe current.*
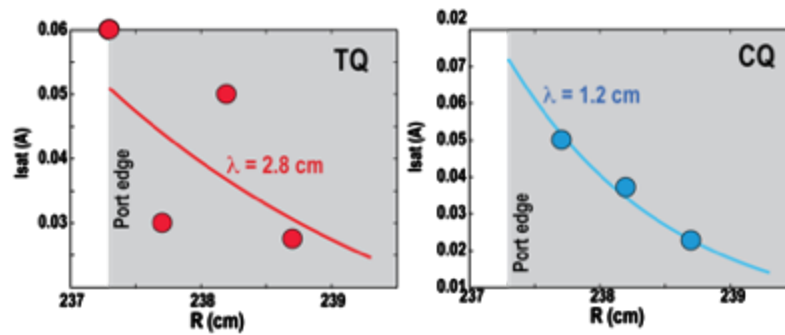
Figure 3.1.5: *Decay length of probe ion saturation current going into the probe port as a function of major radius during the (left) TQ and right (CQ) for 4 repeat shots with different probe positions.*

Converting the single point measurement of Figure 3.1.4 into a global particle sink is quite challenging because the degree of spatial nonuniformity is not known. As a simple estimate for particle balance purposes, we assume a wall area of 20 m^2 (about half of the actual plasma-exposed wall area). Additionally, ions lost along field lines to the divertor, toroidal limiters, and port edges need to be accounted for. To estimate this, the probe position was varied shot-shot for 4 repeat shots. Approximate in-port exponential decay lengths of about 1 – 2 cm were obtained, as shown in Figure 3.1.5, allowing an estimate to be made of plasma lost into the port. To estimate parallel loss in the SOL (to the divertor) and to the midplane limiter, it is assumed that the decay length in these regions is proportional to the connection length (i.e. the cross-field turbulent blob velocity is assumed constant). Connection lengths here are of order 40 m in the SOL, 5 m in the limiter shadow, and 8 cm in the port, so decay is very rapid in the port, but slower in the SOL and limiter regions.
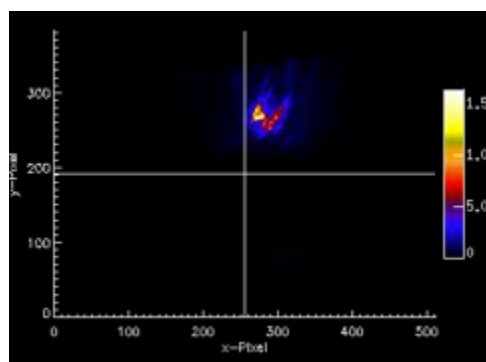

Figure 3.1.6: *Example D imaging of SPI injection port.*

Absolutely calibrated Dα measurements can be used to estimate the ionization source during the shutdown. Here, three different D measurements were made: at toroidal angle Φ = 75º, at Φ = 135º (not looking at the injection port) and Φ = 135º (looking at the injection port). An example of a Dα image looking at the injection port is shown in Figure 3.1.6. Dα brightnesses are

converted into D fluxes using the standard photon efficiency (S/XB) factor. Here, a factor S/XB ~ 50 is used for D in front of the injection port, corresponding to very cold, high density plasma expected in D_2 pellet ablation plumes (T_e = 1 eV, n_e = 10^{15}/cm^3 from ADAS). For non-local D ionization (recycling) we expect the plasma to be warmer and less dense, so a different S/XB ~ 30 is used (T_e = 5 eV, n_e = 10^{14}/cm^3 from ADAS). An integral is done over the whole camera image (for the SPI shard source term), and no attempt is made to separate out gas from shards there, it is simply assumed that shards dominate the signal. For the global ionization terms, a surface area of 20 m^2 is assumed.
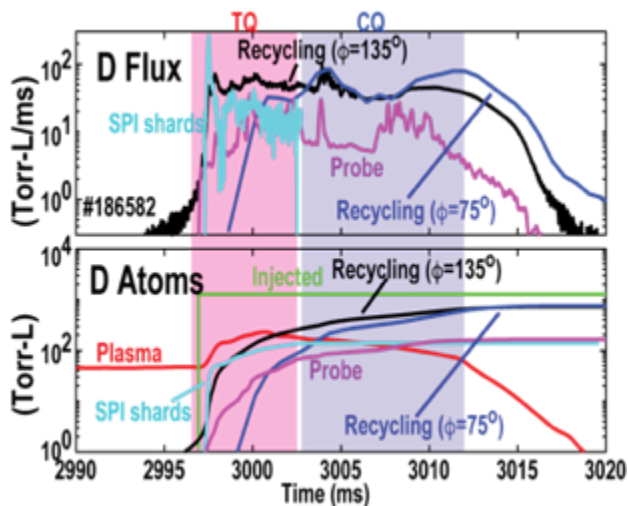

Figure 3.1.7: *Time traces showing estimated particle balance during a D_2 SPI shutdown showing (top) D fluxes and (bottom) D fluences (time integrated fluxes).*

Figure 3.1.7 shows an example of preliminary particle balance for a D_2 SPI shutdown (single SPI from 135°). The top curve shows flux (particles/s) and the bottom curve shows fluence (particle number). It can be seen in the top cyan curve that the first large spike of D ionizations comes, as expected from the injection port ("SPI shards"). The resulting rise in electron number is, within a factor 2, reflected by the plasma inventory (lower red curve, from CO_2 interferometers). By the start of the CQ, the total ionization source from nonlocal sources (recycled gas, lower black and dark blue curves) has passed the local SPI shard source. Although different in magnitude by a factor of 5, the probe and recycling fluences, lower figure, have a similar shape, rising throughout the CQ, while the plasma electron content is dropping. Despite the large uncertainties in the absolute numbers of these estimates, these trends suggest that the CQ electron number is being limited by radial transport. The total ionization source (local plus nonlocal D) does not match the total injected quantity (green curve in lower figure). If every injected D were to interact and ionize, these curves should asymptote to the same value. In a strongly recycling regime, where every D hits the wall and is re-ionized multiple times, the recycling curve should pass the injected curve. The result that the recycled D curve does not reach the injected quantity suggests either inaccuracies from the approximations made

here or, if real, then "gas clogging" where D_2 gas is stuck back in the injection port and never reaches the plasma.

Shot-shot repeatability of mid-CQ D fluence for repeat shots is shown in Figure 3.1.8. Overall, the results are reasonably repeatable, so the disagreement between probe fluence and D fluence appears to be a systematic (not random) error or be a real result illustrating large toroidal variation. An apparent $n = 1$ structure is seen in the data – this can be seen by looking at the D ionization term and the probe sink term (on the other side of the machine) and noticing that the two have a variation which is out of phase. This variation is fairly significant (about a factor of 2 in the probe fluence). There is a $n = 1$ mode seen in the magnetics at the Ip spike, as shown in Figure 3.1.9 (and with phase plotted in Figure 3.1.8).

Overall, the present particle balance work does not give a clear definitive answer as to where the missing D atoms reside during the CQ. Some (but not all) of the discrepancy may be due to toroidal variation in free electron density. Radial flux to the wall definitely exists during the shutdown and is a strong candidate for causing the observed limitation in assimilated particles, as it rises together with global D ionization, with magnitudes large enough to be comparable to the plasma D content. The effect of neutral clogging has still not been quantified however, nor has the number of D atoms hiding in large, slow ice chunks arriving very late in the shutdown (during the CQ or later). Some preliminary evidence for $n = 1$ structure in CQ recycling flux has been observed.
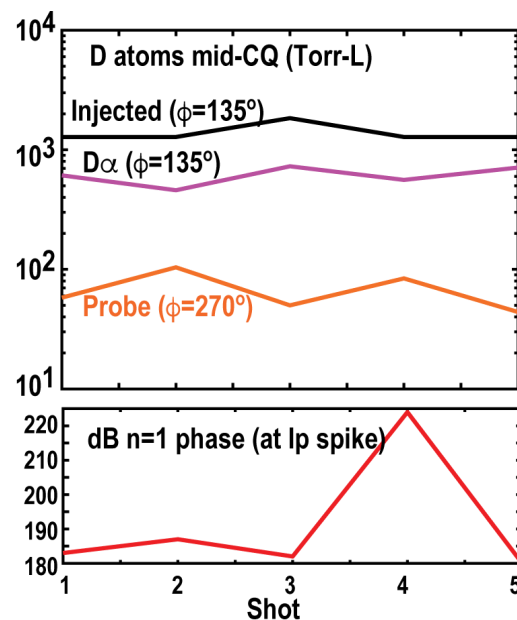

Figure 3.1.8: *Trends seen in mid-CQ D fluence for 5 similar shots, showing slight apparent n = 1 pattern and large apparent asymmetry between injection port location and opposite side of machine, as well as n = 1 phase (from magnetics at outer midplane).*
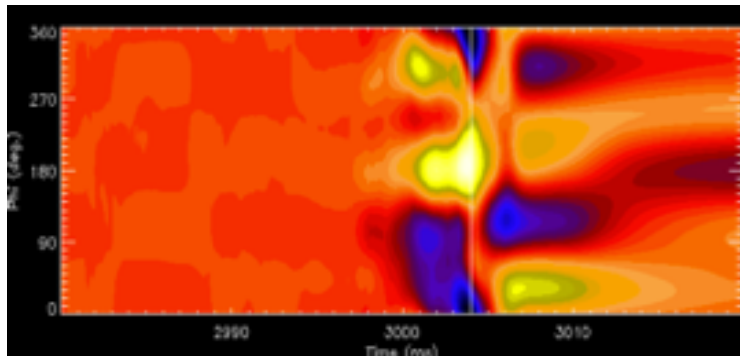
Figure 3.1.9: *Contour plot of poloidal magnetic field at outer midplane vs time with Ip spike shown by white line, showing large n = 1 structure.*

The role of intrinsic carbon impurities in determining the current quench rate following D_2 SPI was studied using controlled non-disruptive injection of carbon granules from the Impurity Granule Injector (IGI) prior D_2 SPI injection in order to modify the carbon impurity background fraction of the pre-disruptive plasma. As shown in Figure 3.1.10, increasing carbon impurity fraction does increase the current quench rate, indicating that the radiative cooling from intrinsic carbon impurities must be carefully accounted for when modeling D_2 SPI shutdowns.
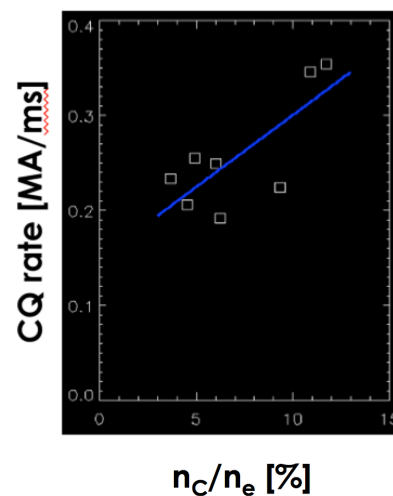

Figure 3.1.10: *DIII-D current quench decay rate as a function of carbon impurity fraction prior to the disruption.*

The role of MHD growth on the pre-TQ dynamics was assessed by a plasma current scan. This allows testing against the MHD threshold of [deVries2016], which finds a critical $n=1$ mode amplitude for triggering the TQ to vary as $\sim q_{95}^{-1.1}$. Analysis of these data indicates that the $n=1$ amplitude is well correlated with the TQ onset, and can explain the observed variability in this timescale. These results (combined with similar analysis from JET and KSTAR) were discussed further in Section 2.3.

3.2 JET

The most recent JET SPI experiments were completed in May 2020, but analysis, modeling, and interpretation of these experiments are ongoing. Some highlights of this work are described here. A further listing of JET SPI results can be found in "Recent Publications from DIII-D, JET, and KSTAR SPI Research (FY 2021)".

JOREK simulations of JET discharges have recently progressed through the majority of the thermal quench (TQ) allowing quantitative comparisons with experiment. Five simulations were launched to scan the Ne/D_2 mix (5, 10, 20, 50, and 100% Ne) in the 8.1 mm pellet size that carries up to 2.46×10^{22} Ne atoms when purely Ne (note there is always a thin D_2 shell on the pellet to facilitate launching). In all simulated cases, high thermal radiated fractions are expected, defined as the TQ radiated energy over the thermal energy (Figure 3.2.1). However in experiment, a 1.5 MJ increase in radiated energy is inferred with Ne quantity, suggesting that low Ne content pellets do not mitigate as well as pure Ne pellets. It should be noted that these radiated energy calculations assume axisymmetry and use a bolometer array that is toroidally opposite the injection location, and therefore changes in the radiation structure could explain the inferred experimental trend. Similar experiments on DIII-D also show an increasing radiated energy with increasing Ne quantity together with a decreasing divertor tile temperature [Shiraki2016], and thus provides more confidence in the validity of this experimental trend. Similar infrared measurements have been tried on JET but low divertor heat fluxes are found for all pellets, independent of the Ne content, though the IR data are subject to large uncertainty due to limited toroidal coverage and background plasma IR radiation. Possible conclusions are: (1) the divertor heat flux is toroidally localized away from the divertor IR views in the cases with low neon content, (2) significant energy is conducted/convected to the first wall in the cases with low neon content, or (3) the inferred radiated energy trend is an artefact of the calculation and all pellets do in fact mitigate the thermal energy well.
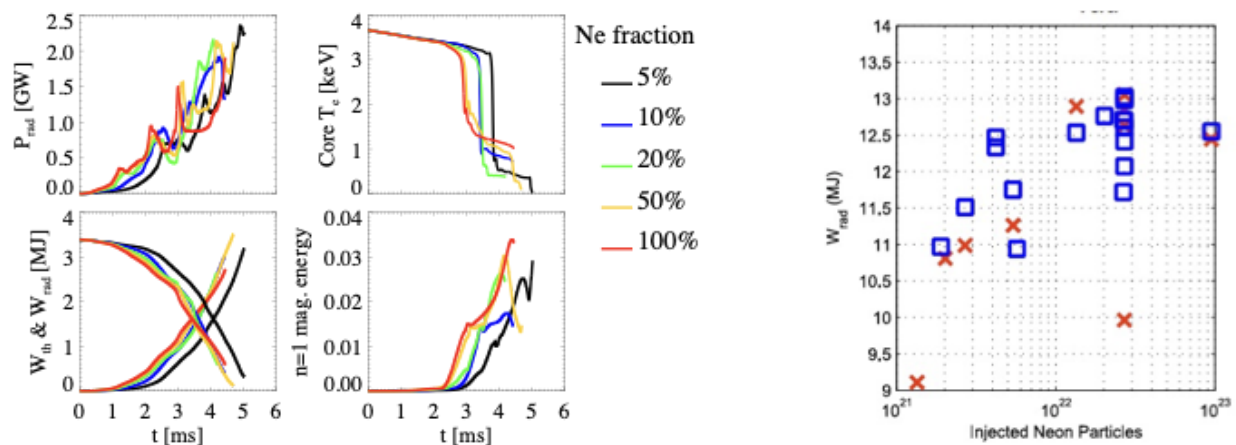

Figure 3.2.1: *(left) JOREK simulations of the Ne fraction scan in the 8.1 mm pellet. The times span from material arrival almost through the end of the TQ. JOREK simulations courtesy of D. Bonfiglio. (right)*

Experimental measurements of the radiated energy during the full disruption (TQ + CQ) using the horizontal bolometer array far from the injection and assuming axisymmetry. Blue squares indicate pellets that were mechanically punched and red crosses are without the punch.

Given the uncertainties in the standard bolometer analysis, work has been ongoing to develop 3D inversion techniques with error analysis in a code package called Emis3D [Sweeney2020]. The limited bolometer coverage in JET is not expected to well constrain the 3D structure, but doing this analysis will provide a significant improvement on the understanding of the radiation structures and will place error bars on the radiated energy estimates. Further, the code is intended to be portable to machines where the 3D structure can be better constrained.

The JOREK simulations show a clear 2/1 radiation structure during the TQ (see Figure 3.2.2 right). Part of the 2/1 flux tube intersects the injection trajectory and therefore the radiation is consistent with where the Ne is deposited. Experimental poloidal maps of reduced chi-squared are produced showing which helical phantoms are most likely to explain the bolometer data. Each cross represents a single helical phantom with a bivariate Gaussian profile in the poloidal plane. The contour on the left of Figure 3.2.2 shows a region of low reduced chi-squared below the magnetic axis. Within Emis3D, this helical phantom is traced for ¾ toroidal transit in either direction, which if traced for another ¼ transit, would intersect this poloidal plane again. The region of good fits (i.e. red) is seen to extend in towards the core and outwards towards the expected location of the q=2 surface. The second q=2 flux tube would intersect the poloidal plane approximately where the red oval is placed. We conclude that the radiation structures show some qualitative agreement in the poloidal plane, with a dominant region located below the magnetic axis. Some radiation would be expected in the flux tube above the magnetic axis in experiment. To assist in code validation, an interface between JOREK and Emis3D is in development that will provide an estimate of the likelihood that the simulation is predicting the experiment.
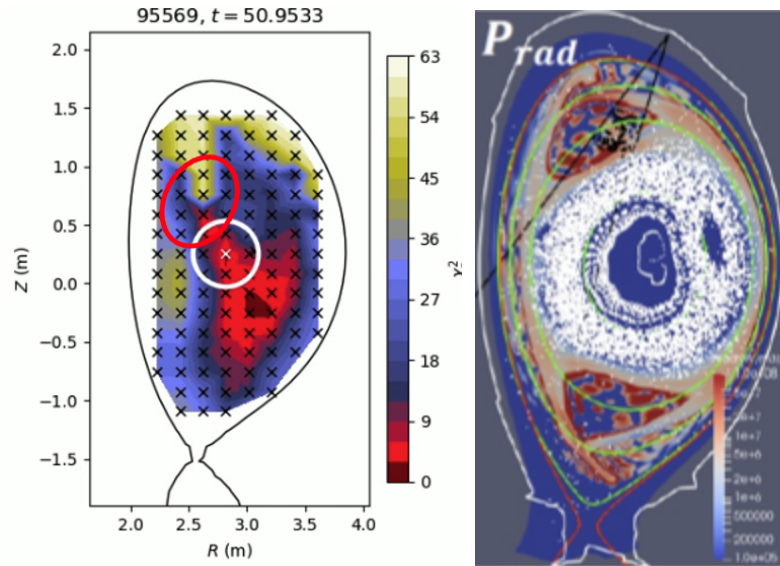
Figure 3.2.2: *(left) Experimental map of reduced chi-square at the time of the thermal quench showing the most likely location of the radiation in the poloidal plane at the injection location. One toroidal transit of the flux tube marked in dark red maps to the location of the red oval. (right) JOREK simulation of the peak radiation at the thermal quench for the same discharge.*

While some qualitative agreement is seen in the poloidal distribution of radiation, there are clear discrepancies in the toroidal radiation profile (see Figure 2.2.3 and surrounding discussion).

A comprehensive summary of the thermal mitigation experiments is reported in [Sheikh2021]. JET radiation over the entire disruption saturates at high neon quantities, and this is interpreted as being due to high fractions of W_{th} being radiated, with differences in magnetic energy leading to the significant changes in W_{rad} across plasma scenarios [Sheikh2021]. This is measured with foil bolometers, and accounts for radiation asymmetries based on Emis3D interpretive modeling. Infrared cameras observing the JET divertor show low conducted heat fluxes, which is qualitatively consistent with a high radiated fraction, as described previously.
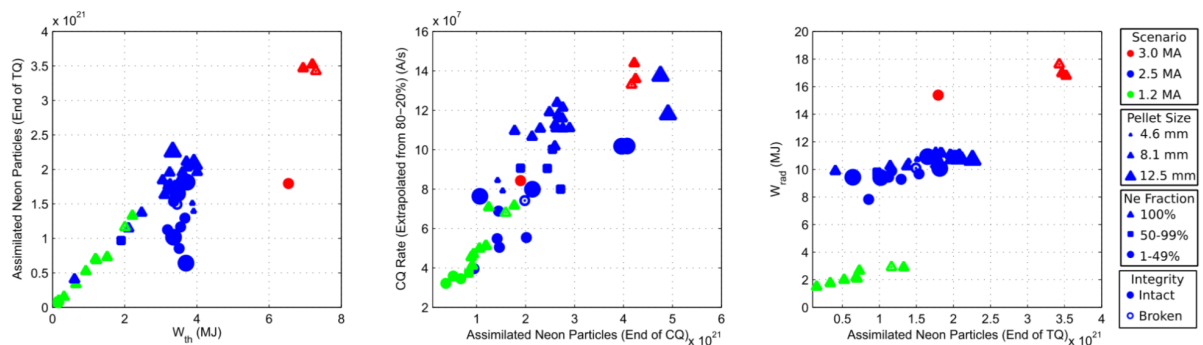

Figure 3.2.3: *Assimilation of injected neon is driven by available thermal energy (left and center), and leads to high observed radiation fractions (right) of the thermal energy, leading to radiation depending primarily on the magnetic energy. From [Sheikh2021].*

3.3 KSTAR

KSTAR experiments with the dual midplane SPI systems (similar to the planned ITER configuration) separated toroidally by 180° are still ongoing. After an initial SPI systems checkout in January 2020, a multi-day experimental campaign was executed in Fall 2020, although with limited disruption diagnostic coverage due to failures in multiple new diagnostic systems. A second campaign with improved diagnostics coverage, is underway as of this writing in August and September 2021. Newly functional disruption diagnostics in 2021 include a fully operational dispersion interferometer for measuring SPI density perturbations, fully functional filtered poloidal AXUV arrays and partially functional toroidal AXUV arrays for measuring SPI radiation asymmetries, and a visible fast imaging diagnostic for determining pellet integrity in the guide tube. Collection and analysis of the new 2021 data is very preliminary and remains an active effort.

New KSTAR SPI data from the 2021 campaign includes the first measurement of toroidal density asymmetries resulting from pure D2 SPI from injectors 180° apart. This measurement was enabled by upgrades to the new dispersion interferometer system to minimize vibrations in the system that prevented accurate density measurements through most of the 2020 campaign. As shown in Figure 3.3.1, the density rise resulting from the G-port SPI alone (blue, G-port located toroidally very near to the interferometer) rises slightly sooner than the O-port SPI alone (green, O-port located 180° away toroidally), but they are roughly identical within a couple milliseconds (accounting for a baseline shift), indicating rapid symmetrization of the injected D2 particles.

The fully operational dispersion interferometer also provided indication that multiple SPI can be successfully superimposed to increase the total particle assimilation in the plasma. As shown in Figure 3.3.2, D2 pellets injected from G-port and O-port synchronized to arrive at the plasma edge within 0.9ms of each other exhibit a significantly higher density spike than larger delays (+2.1 or +3.8ms). The observed density rise is significantly smaller when O-port precedes G-port than vice versa, suggesting a sensitivity of the measurement to the interferometer chords relative to the first arriving pellet, as the dispersion interferometer is much close to G-port than O-port.
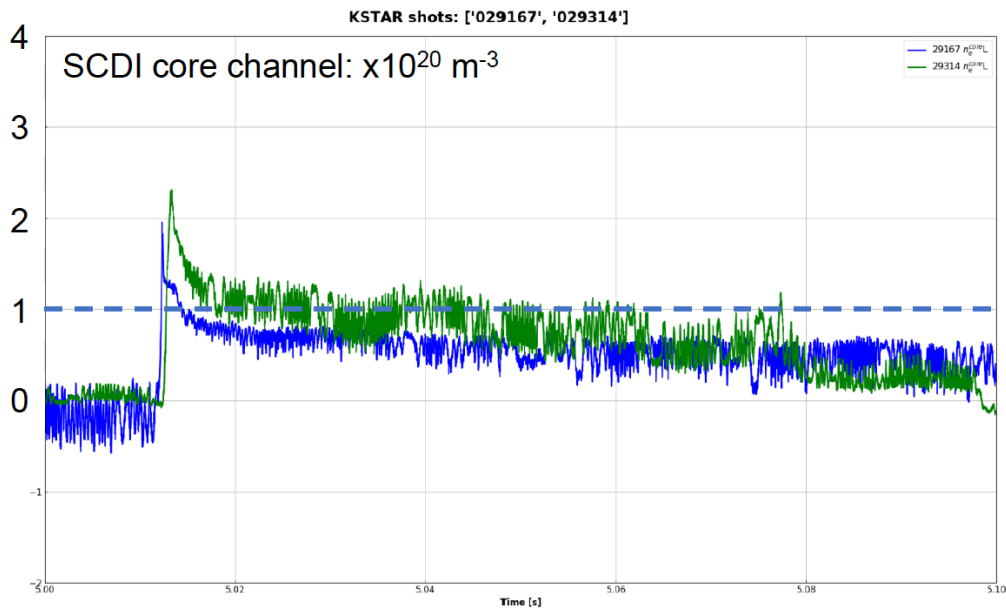
Figure 3.3.1: *Comparison of core density signals measured during the injection of a pure D2 pellet from the G-port (blue) and O-port (green) SPI. Accounting for the baseline offset, the signals exhibit near axisymmetry within a couple milliseconds of the initial density spike.*
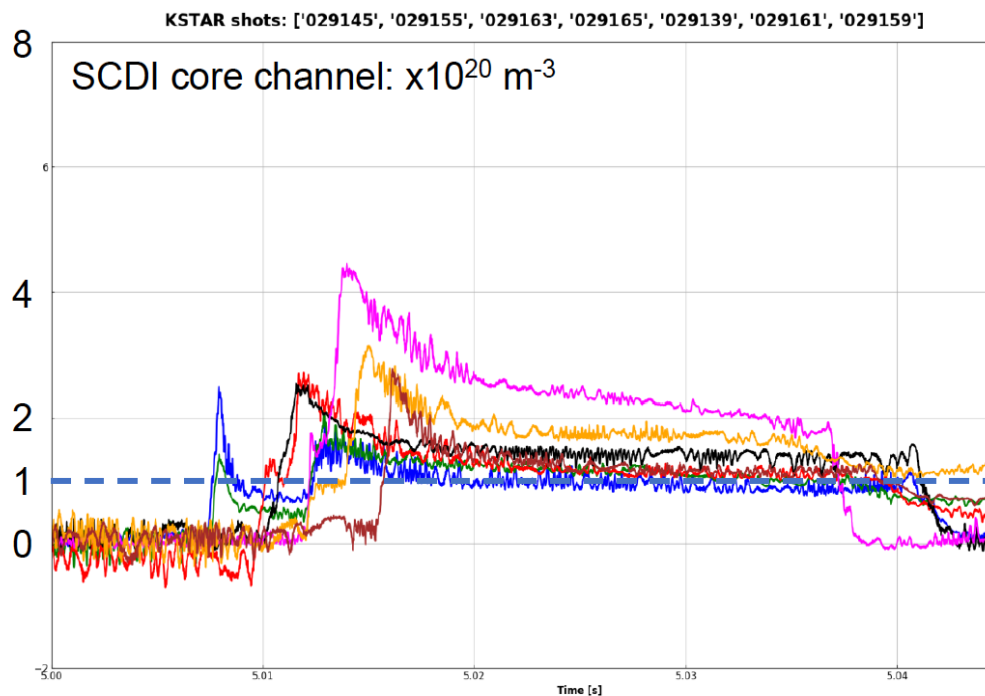

Figure 3.3.2: *Density perturbations resulting from the injection of D2 SPI from G-port and O-port with varying relative delays. Delays (O arrival time relative to G arrival) = +0.9ms (pink), +2.1ms (orange), +3.8ms (brown), -1.2ms (red), -4.2ms (green), -4.5ms (blue).*

31

The new pellet imaging diagnostic has been used in an attempt to correlate pellet integrity with the resulting particle assimilation. This diagnostic allows more detailed observation of the in-flight integrity of the SPI pellets (whole, broken, shattered) than the microwave cavity systems in place in SPI system on DIII-D and JET, as well as the previous microwave cavity on the KSTAR SPI. Examples of the pellet integrity resolution and resulting plasma density response for cases with shattered, wholem, and partially broken pellets are shown in Figure 3.3.3. Any correlations as to the effectiveness of the SPI under varying levels of in-flight breakage are too preliminary at present to make definitive statements.
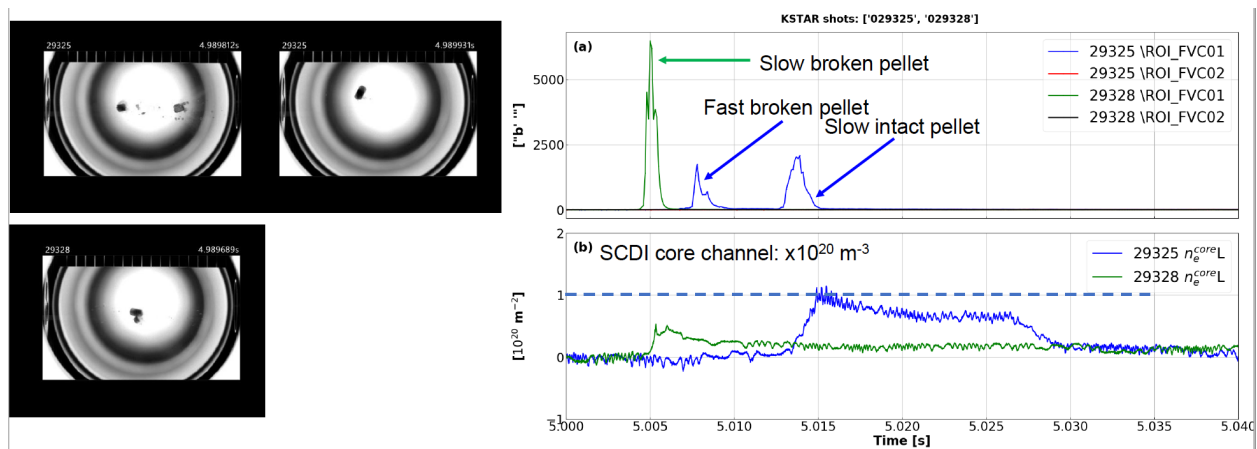

Figure 3.3.3: *Left: Visible camera images of D2 SPI in the flight tube, corresponding to a dual SPI case (top) and single SPI case (bottom). The plasma density response is shown in teh bottom right, with blue corresponding to the top left dual SPI case and green to the bottom left single SPI case.*

A single SPI was used to investigate the disruption characteristics for varying neon (Ne) to deuterium ratios in the injected pellets. The maximum achievable Ne:D$_2$ ratio is 85:15, as a thin D$_2$ layer around the Ne pellet is required for successful pneumatic launch, precluding pure Ne injection without a mechanical punch. As can be seen in Figures 3.3.4a-b, the cooling duration, defined as the delay from first arrival of SPI fragments at the plasma edge to the TQ, decreases as the Ne fraction increases due to strong radiation from the injected Ne. On the other hand, in the case of the 7.0 mm pellets, it can be seen that the current quench (CQ) duration is almost saturated for neon fractions of 15% or more (Figure 3.3.4c). Additionally, in the case of small neon fractions, the CQ duration varies widely, as also observed on DIII-D. This is believed to be caused by the influence of intrinsic carbon impurities from the wall when the plasma is cooled by dilution.
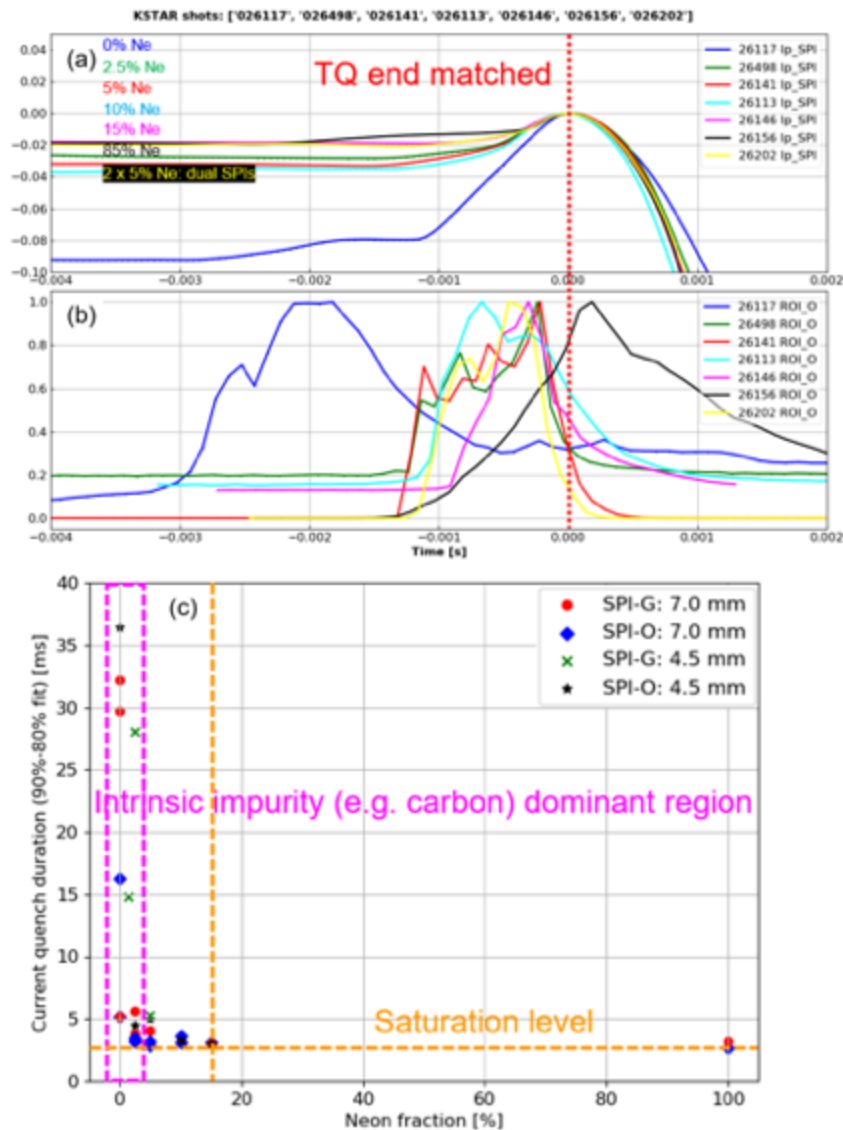
Figure 3.3.4: *(a) Plasma current waveforms near TQ end (time adjusted to TQ end based on Ip spike), (b) CCD intensity waveforms near injection point by region-of-interest (ROI) sum, and (c) CQ duration of single SPI (extrapolation with dIp/dt rate during 90%-80% of plasma current). (a) and (b) are the results for 7.0 mm pellets, but (c) also includes the results for 4.5 mm.*

Multiple SPI from two different toroidal locations were utilized to study the effect of pellet synchronization upon mitigation parameters. No correlation of cooling duration with the level of synchronization was observed (Figure 3.3.5a-c). On the other hand, in the case of multiple injections, including quadruple injection, a small reduction in the CQ duration is observed in highly synchronized cases, in comparison to asynchronous cases. Figure 3.3.5d shows CQ times for single, dual and quadruple injections with the same total number of 2.3×10^{21} Ne atoms. The data confirms some additive effect from multiple Ne injections.
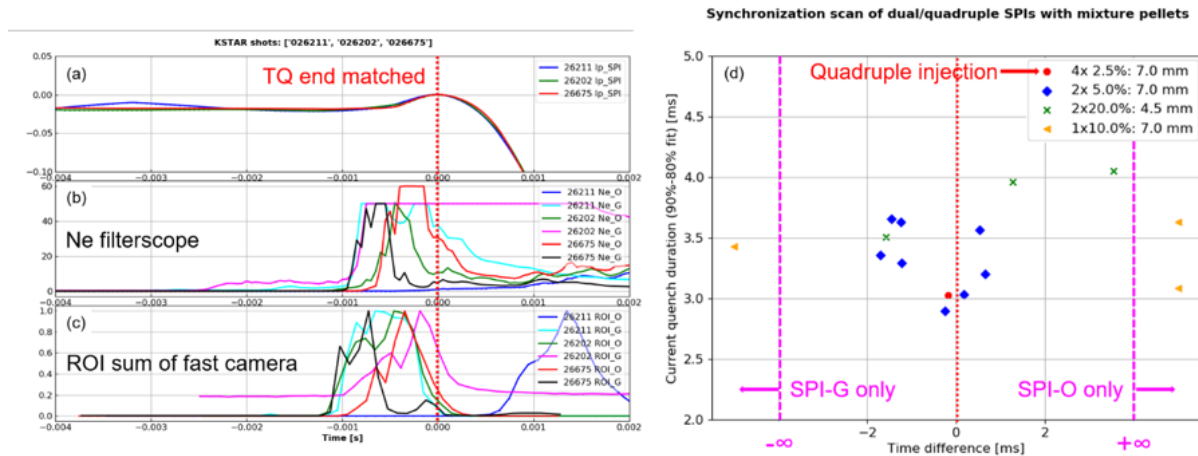
Figure 3.3.5: *(a) Plasma current waveforms near TQ end, (b) neon filterscope waveforms, (c) CCD intensity waveforms near injection point by ROI sum, and (d) CQ duration of single SPI (extrapolation with dIp/dt rate during 90%-80% of plasma current).*

The amplitude of the n=1 MHD mode triggered by SPI differs depending on the level of synchronization. This indicates that the TQ process is impacted by the pellet arrival time, which can then also influence for example the radiation level and distribution. Strong radiative cooling can create a strong MHD mode in the plasma. Conversely, this MHD mode has a significant impact on the behavior of the injected particles (e.g., the mixing of injected particles). As shown in Figure 3.3.6, well-synchronized dual SPIs result in a lower n=1 mode amplitude with shorter lifetime compared to the asynchronized SPIs. Preliminary numerical analysis of the SPI-induced MHD mode (not shown here) indicates that the symmetrical injection of two SPIs causes negligible odd perturbations (e.g., n = 1) and causes significant even perturbations (e.g., n = 2).
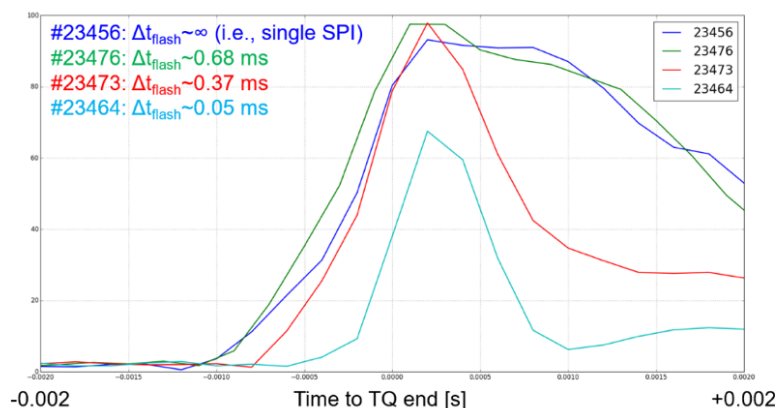

Figure 3.3.6: *n=1 mode amplitude waveform depending on the synchronization.*

Comparing #23456 (single 5% neon-doped pellet) and #23464 (dual 5% neon-doped pellets), #23464 shows a shorter cooling duration due to the larger total amount of neon (equivalent to

10% neon-doped pellet). On the other hand, the n=1 amplitude is the weakest among the shots in Figure 3.3.6.

The ITER disruption mitigation system will consist of many SPI barrels located at a small number of toroidal locations. The additive effect of the multiple barrel injection at the same toroidal location was investigated by replacing the existing 8.5 mm barrel with a 7.0 mm barrel and combining it with the existing 7.0 mm barrel. As shown in figure Figure 3.3.7, as the time difference between the pellet arrival decreases, the CQ duration tends to decrease, similar to the multiple SPI cases from different toroidal locations.
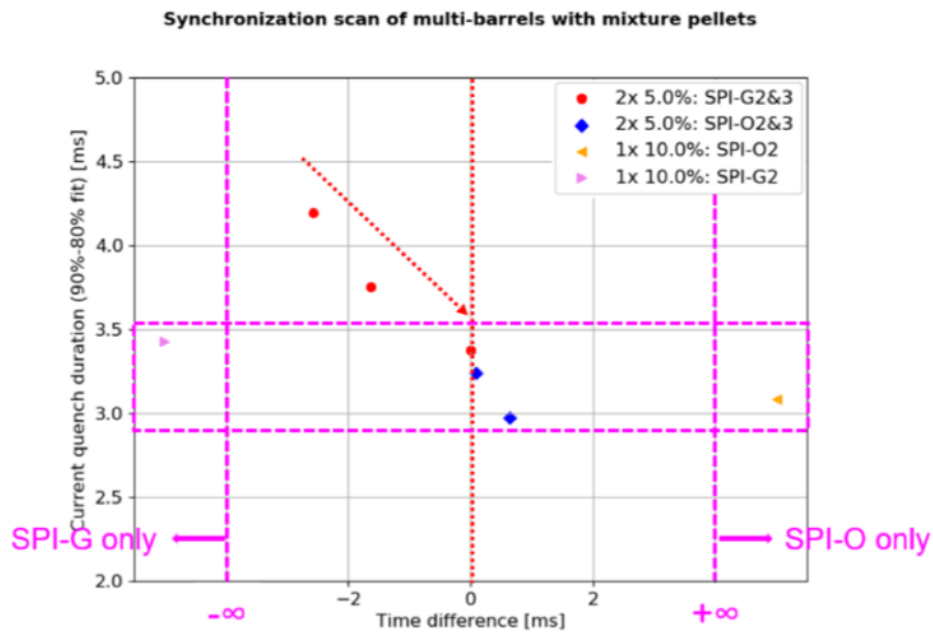

Figure 3.3.7: *CQ duration of multi-barrel SPIs (extrapolation with dIp/dt rate during 90%-80% of plasma current).*

4. Remaining Gaps and Questions

As described in Section 2, several areas of study exhibit common understanding across the facilities, and represent areas of relatively mature understanding. However, in other areas, significant key questions remain to be resolved. These areas, their current level of understanding, and suggestions for future work on these topics are given.

4.1 Effect of distributing particle source over multiple injectors

SPI shutdowns in ITER will utilize multiple toroidally separated injectors, due to both the large required throughputs and the desire for symmetry. The implications of distributing an injection across multiple ports is not yet fully understood.

In the case of high-Z or mixed-species (with significant high-Z fraction) shutdowns, KPRAD successfully matches DIII-D experiments with two toroidally separated injections [Herfindal2019]. The modeling in these cases account for the effect of mismatched timing, and can reproduce observed trends. Thus in such cases the dominant role of impurity radiation allows a 0D picture to describe the basic physics. However, notably in these cases, cooling durations are not matched, indicating that some 3D effects related to the multiple injection sources do exist. Furthermore, radiation asymmetry reduction is also not fully clear, with preliminary results only giving qualitative indications that peaking may be reduced.

For pure deuterium injection, the effects of radial transport may further complicate the ability to superimpose the density rise from each individual pellet. Additional discussion of this related topic follows in Section 4.2.

Although understanding of this multi-SPI physics is among the high-level goals of the KSTAR SPI research, a similar explicit focus utilizing the dual-SPIs should be a specific focus for future DIII-D work. Because toroidal resolution for radiation diagnostics are discrete (even when toroidally distributed), data to constrain such distributions can be maximized by combining information from both the 180 degree KSTAR configuration and the 120 degree DIII-D configuration.

4.2 Predictive understanding of hydrogenic SPI radial transport

While experimental evidence of radial transport is clearly seen in DIII-D (as described in Section 3.1), a quantitative and predictive capability is lacking. This is essential for understanding the level of core densification and RE dissipation to be expected. Whether RE beams can be fully suppressed, or of the magnitude of a beam if avalanching does occur (and the dependence of this on plasma current), are dependent on this understanding.

This topic is an area where the currently available predictive tools may be insufficient. The 0D KPRAD model is unable to resolve this physics since it does not contain spatial information. On the other hand, it is challenging for full 3D extended MHD codes to provide the level of "fitting" required to quantitatively match observed profiles to assess the responsible radial transport. Rather, reduced modeling of an intermediate scope, with the necessary geometry (at least 1D in the radial direction), is required.

The 1D INDEX model [Matsuyama2021] provides such a capability, with the necessary geometry as well as sufficient model reduction to allow adjusting of radial transport parameters to compare predicted profile evolution with the detailed density profiles collected by TS in DIII-D. This comparative study is enabled by the low-T_e polychromaters, allowing the post-injection profiles including open-field line regions, to be measured. This comparative collaboration between DIII-D and QST in Japan has been initiated in summer 2021, and continuation of this effort is strongly encouraged for progress in this area. Ultimately, success with this 1D reduced modeling can provide input for specifying transport in the more complete 3D codes. This is likely required due to the observed importance of MHD growth in the disruption dynamics for these hydrogenic injections.

4.3 Ideal shatter plume

The penetration of injected particles into the plasma core is a function of the solid/gas fractions within the SPI plume along with the fragment size distribution of the solid pieces. Accelerating the pellet as a solid then shattering it at the end of the guide tube (just prior to entering the plasma) allows a rapid particle delivery without the temporal spreading that occurs with an MGI pulse traveling down a tube [Baylor2015]. However, depending on the bend angle and geometry of the shatter tube and the pellet impact energy, a significant fraction of the SPI plume can ultimately end up as a gas or fine mist of tiny particles.

Early work at ORNL and DIII-D iterated on the design of the shattering mechanism [Combs,Commaux], but subsequent installations (the second SPI on DIII-D as well as both systems on KSTAR) have followed a similar design [Meitner2017,Baylor2021], and the JET shatter tube was only slightly modified due to spatial constraints in the port [Baylor2021]. Recent work has used fast camera imaging from laboratory tests to characterize the resulting fragment size distribution, and developed an impact energy-based model for this distribution [Gebhart2020].

The variation of this shatter plume distribution represents one of the few remaining areas for optimization within the ITER DMS design, and leads to two key questions: How can a particular fragment size distribution be generated, and what type of distribution is optimal for plasma shutdown characteristics?

The former issue, on production of an SPI plume with desired fragment size distribution, can largely be studied in the laboratory, as with the approach taken in [Gebhart2020,Gebhart2021] or by similar techniques. The engineering studies likely to provide timely input for the ITER design are currently underway [Gebhart2021,Luce2021].

The latter question of optimal distributions is more complex, depending additionally on plasma physics. 3D extended MHD simulations have assumed a number of shatter size distributions, ranging from uniform size to a single monolithic particle, and report only modest differences in TQ characteristics [Kim2021]. However, no experimental studies of this question exist to date.

Recently, ASDEX-Upgrade has initiated an SPI research program with a primary focus to investigate such effects, incorporating a number of available shatter tubes that can be installed simultaneously. This program, which is a collaborative effort with the ITER Organization and through the ITER Disruption Task Force, is completing SPI installation with experiments anticipated to begin in 2022. US involvement in this scientific program would be of great benefit in improving understanding of this currently unresolved topic of study, and represents the likeliest path to helping constrain the issue of shatter plume characteristics and its effect on mitigation metrics.

4.4 Runaway electron seed formation

The production of some seed runaway electrons during a SPI TQ has been observed in DIII-D, particularly at high T_e [Hollmann2020]. Detailed understanding of the scaling of this effect with neon fraction is a critical issue, as the thermal mitigation and RE mitigation aspects are closely coupled. In addition to tuning the CQ rates (which must be fast enough to mitigate halo current forces but slow enough to avoid excessive eddy current torques), rapid radiative cooling has opposing effects for the thermal and RE mitigation aspects. Strong radiation due to high-Z impurities is beneficial for lowering conducted heat loads, but may lead to hot-tail generation of RE seeds. Optimal delivery will require relatively small neon fractions, where disruption dynamics depend most sensitively on this quantity [Shiraki2016], making optimization of high-Z impurity quantities critical.

Part of the challenge in this area is related to diagnostic capability, due to the relatively small seed RE populations observed during SPI in current devices. Several promising approaches have been proposed that may improve this detection capability. The use of TS spectra to detect early generation of non-thermal electrons during the SPI shutdown has shown promise [Hollmann2020], and should now be more widely applicable in DIII-D. Additional diagnostics for early low-energy RE seeds, such as an EUV camera (for REs in the 10's of keV range) could provide additional capability with greater spatial resolution, but would require investment from one of the SPI-equipped facilities for implementation. The potential transport of these early

seeds (due to TQ or early-CQ MHD modes, for example) is related to the above issue of thermal plasma transport during low-Z SPI, and also requires further understanding.

4.5 Runaway electron benign termination

The benign termination of a RE beam through the injection of D_2 together with crossing a global MHD stability boundary, is a relatively new approach to RE mitigation. Because the mitigation action takes place only after a high-energy beam is already formed, the technique carries significant risk, and important questions remain regarding its practical application in ITER. Moving forward, additional work is needed to assess the critical D_2 injection quantity needed for this approach, as well as the consequence of injecting too much D_2, which increases collisionality. Additional work with H_2 injection into Ne dominated RE beams is needed. Further study of the compatibility of large-scale MHD excitation during vertically unstable RE beam evolutions is needed. These studies are planned to be proposed during future experimental campaigns.

5. Other JRT Activities

As part of the JRT, related topics have been studied, in the areas of alternative injection techniques and UFO disruptions. While not specific to SPI physics, these areas are relevant to the overall disruption topic and address or identify possible gaps in the SPI mitigation approach. The activities in these areas are summarized here.

5.1 Alternative injection techniques

Because of the significant challenges for effective disruption mitigation in ITER, and possible gaps in SPI performance (discussed earlier), comparisons to other techniques remain important. Other disruption mitigation techniques studied here include pneumatically propelled diamond-shelled dispersive pellets containing boron dust, and electromagnetic pellet injection of a solid or shell pellet. The goal of these alternative techniques is to achieve greater penetration and/or increased central cooling as opposed to edge cooling. This could lead to increased efficacy in a plasma with the size and parameters of ITER.

5.1.1 Inside-out shell deposition

The dispersive shell pellet (DSP) injection technique [Hollmann2019] is envisioned to have certain key advantages over SPI, including higher radiated energy fraction without the need for large quantities of high-Z material, less runaway electron production and a slower current quench that remains away from lower bounds set by eddy currents. The technique relies on ablation of a low-Z hollow shell in the plasma edge, releasing the dispersive, radiating payload in the core. Among the potential disadvantages of the technique relative to SPI is the technical challenge of rapidly accelerating a thin-walled DSP, and the robustness of the payload delivery to changes in the target plasma, including situations of a TQ already in progress.

Recent simulations of DSP with NIMROD [Izzo2021] have sought to reproduce the experimental trends vs. pellet speed found in [Hollmann2019], and can also be compared with NIMROD SPI simulations in key mitigation metrics. For the NIMROD DSP simulations with the payload released closest to the center, shown in Figure 5.1.1., the radiation fraction exceeds 90% (the target threshold for thermal quench mitigation in ITER), and significantly higher than similar NIMROD SPI simulations in the vicinity of 50% (as stated in the Q1 report). This high radiation fraction is attributed to the low ablation of the shell, and hence minimal perturbation in the edge of the plasma. Although some pre-TQ MHD is triggered by the shell material, this occurs in the core where more shell material is ablated, while the edge flux surfaces remain intact. Even for slower pellets releasing the payload slightly further from the core, radiation fractions of >85% were found.
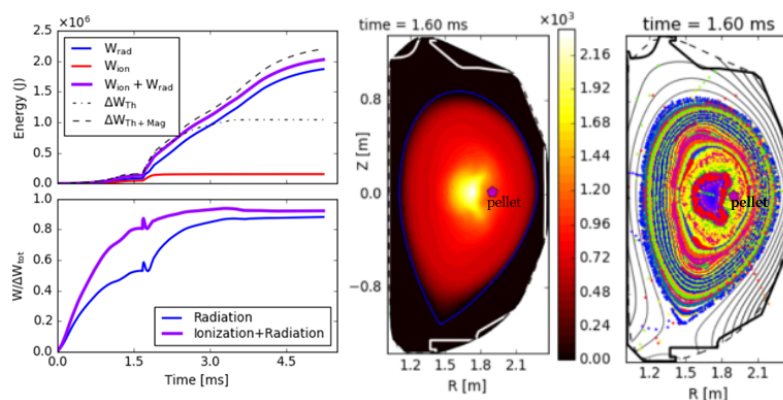
Figure 5.1.1: *(Upper left) Total energy into radiation and ionization compared with total loss of thermal and magnetic energy in a NIMROD shell pellet simulation. (Lower left) Radiated energy fraction calculated from curves above. (Center and Right) Temperature contours and field-line Poincare plots as the pellet approaches the center (just before payload release).*

Another proposed advantage of DSP over SPI is the prospect of less RE production due to slower cooling by low-Z material, possibly with a higher final T_e. Experiments, however, showed indication of RE production and prompt loss for the deepest penetrating pellets [Hollmann2019]. The simulations likewise predict rapid cooling into the E>E$_{crit}$ regime for well centered pellets, such that hot-tail RE generation would be expected [Izzo2021]. These findings indicate that more careful optimization of the payload might be required to capitalize on this promised advantage. DSP may possess some advantages over SPI with respect to deconfinement of REs on stochastic fields. A comparison of MHD mode activity in the two cases requires further study, but DSP simulations indicate that, in the case of inside-out cooling, the last phase of the TQ and the plasma current spike are triggered by a 3/1 double tearing mode with a broad radial structure producing a large stochastic region in the edge [Izzo2021]. This appears to differ significantly from the phenomenology of a SPI TQ and I$_p$ spike.

5.1.2 High-speed injection techniques

As another alternative to SPI, an electromagnetic pellet injection (EPI) mechanism has been recently proposed [Raman2019]. The EPI system accelerates a sabot electromagnetically with a rail gun. The sabot is a metal capsule that can be accelerated to high velocities. At the end of its acceleration, the sabot will release the radiative payload that is composed of granules of low-Z materials, or a shell pellet containing smaller pellets. The proposed EPI in this study is predicted to offer a fast response time and high enough speed to deposit the payloads in the plasma core in ITER prior to TQ onset.

The objective of the EPI / Shell Pellet method is to cool the core prior to cooling the outer regions of the plasma to generate an inside to outside thermal quench, and if that could be

41

achieved before the pellet gets to the core, that that is certainly a desirable result as it would ease the requirements on the pellet velocity needed for deep penetration in high-power reactor plasmas. This was planned to be achieved by depositing the radiative material directly in the core. These simulations suggest that cooling of the core is achieved by magnetic field lines in the core connecting to the injected plasmoid cloud before the pellet reaches the core. While this itself is not undesirable, additional studies are needed to understand if this mechanism applies only to discharges without a q=2 surface (the present L-mode case) or also to H-mode discharges with a q=2 surface.

To explore the EPI concept and its potential benefits, we have conducted a series of simulations modeling injection of a single carbon pellet in NSTX-U with the M3D-C1 code [Clauser2021].
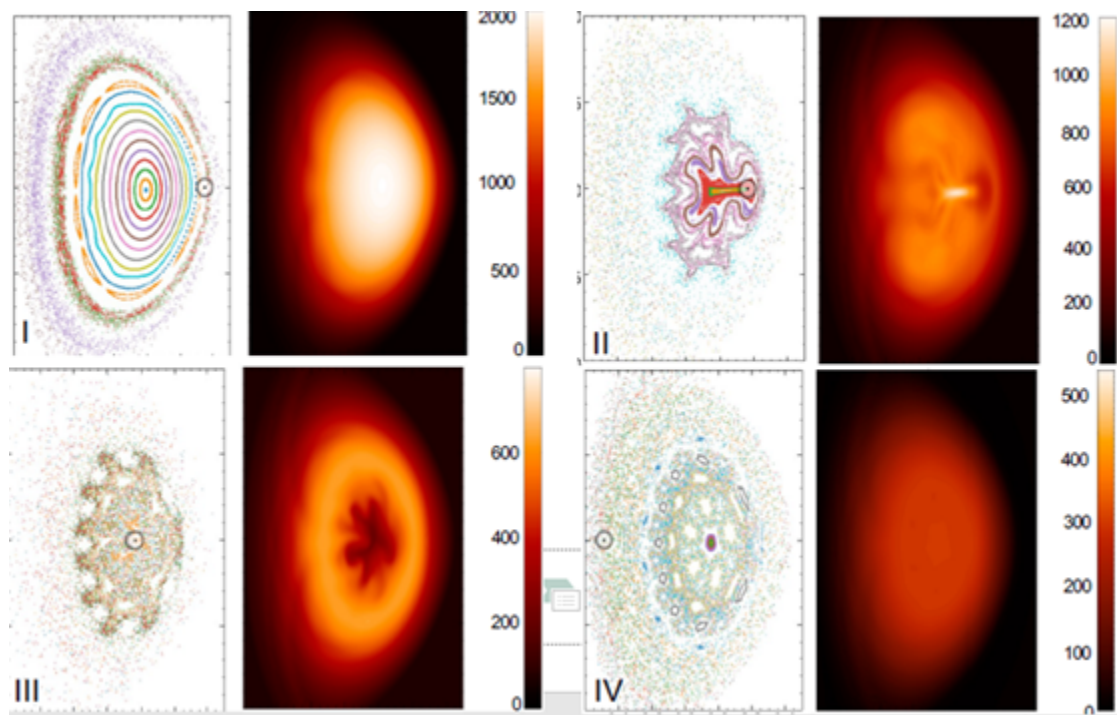

Figure 5.1.2: *M3D-C1 simulation of EPI injection into a NSTX-U plasma displaying Poincare and 2D plasma electron temperature contours for four time points (I = 0.1, II=0.2, III=0.4, IV=1.0 ms after pellet arrival at plasma edge).*

Shown in Figure 5.1.2 are Poincare plots and 2D plasma electron temperature for times I-0.1 ms, II-0.2 ms, III-0.4 ms and IV-1.0 ms for a 1000 m/s 1mm carbon pellet injected into NSTX-U. Also shown on the Poincare plot is the location of the pellet. The Poincare plot in frame II shows that the surfaces in the center are destroyed well before the pellet reaches the magnetic axis. This leads to rapid reduction of the central temperature even before the pellet reaches the center. This speed of 1000 m/s is too rapid for the pellet to fully ablate in NSTX-U. We have also modeled pellets with velocities of 300 m/s and 500 m/s and have modeled tangential injection (as opposed to radial as shown in the figure) to increase the amount of carbon ablated. In

NSTX-U, decreasing the velocity to 500 m/s (or 300m/s) increases the radiated power, normalized to the velocity, by a factor of 1.6 (or 2.3 respectively). By using a hollow pellet with a radius of 3.6 mm, but with the same amount of carbon as in the 1 mm pellets shown in the figure and by injecting tangentially rather than radially, we were able to increase the amount of ablation for a 1000 m/s pellet from 11% to 32%, with a corresponding increase in the amount of radiated power. These results demonstrate that assimilation and global metrics such as the radiated power are sensitive to the pellet speed (via its influence on deposition location), and motivate a need for higher-speed delivery in future large, high-temperature reactor plasmas.

5.2 Alcator C-Mod Analysis of UFO Disruptions

Although unplanned, UFO events are a form of impurity injection that bears some resemblance to the injections used for disruption mitigation. Therefore, one might expect that UFO disruptions are less damaging than other types such as locked modes, vertical displacement events, density limits, etc. Such a finding (if found to be true) would be potentially beneficial in that it would ease the demands of a disruption mitigation system (DMS) in protecting against this type of disruption cause. This hypothesis has been studied based on archived data from Alcator C-Mod.

Tokamaks with a high-Z metal first wall (molybdenum in Alcator C-Mod; tungsten in JET-ILW, AUG tungsten coated tiles, DIII-D tungsten metal ring campaign, molybdenum and tungsten in EAST) experience sudden injections of grain-size flecks of the high-Z wall material. The high-Z impurities penetrate into the hot plasma, rapidly become highly ionized, and can then radiate prodigious amounts of the plasma thermal energy extremely quickly. In Alcator C-Mod, the rapid thermal loss from these so-called "UFOs" were found to trigger about 25% of all flattop disruptions. These disruptions are characterized by sudden, large increases in line radiation from highly charged states of molybdenum (Mo XXXI - Mo XXXIX, observed with a flat-grating spectrometer having 2 ms temporal resolution), as well as sudden, large increases in the total radiated power (observed with MHz-sampled AXUV bolometers). No other C-Mod diagnostic signals showed any disruption-relevant indications prior to the UFO injection (i.e. no locked modes, vertical instability, tearing modes, profile changes, or confinement degradation). The timescale for this UFO disruption-triggering process was typically only 1-5 ms in Alcator C-Mod, so these disruptions were essentially impossible to predict in advance with a useful warning time [Rea2018, Zhu2021], and therefore not able to be avoided or mitigated.
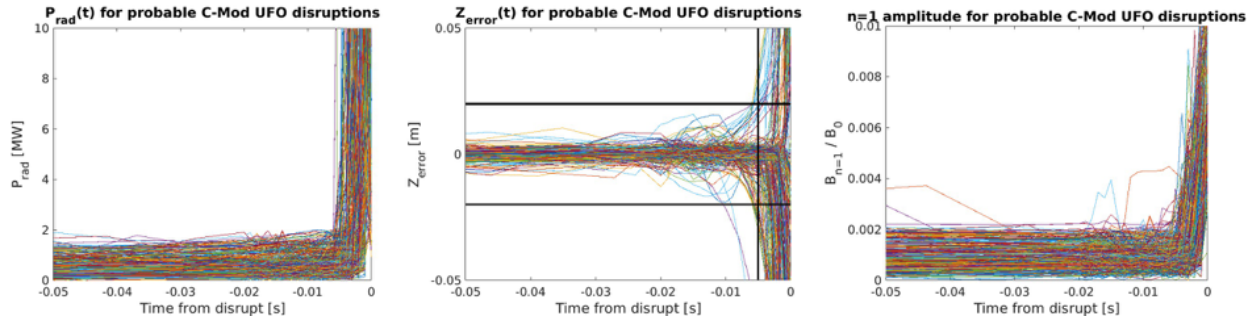
Figure 5.2.1: *(left) Radiated power time traces for UFO events in Alcator C-Mod. Also shown is the error in the vertical position (center) and the n=1 magnetic amplitude (right).*

It is likely that poor tile alignment and the existence of unshadowed tiles are the causes of these UFO injections. Fast ion impacts might also play a role in sputtering wall material. Clear evidence of tile melting that "does not require a microscope" to see is shown in Figure 5.2.2.
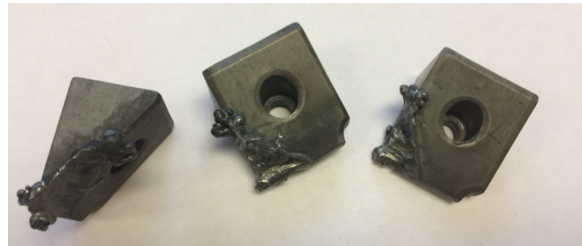

Figure 5.2.2: *Three molybdenum tiles removed from the Alcator C-Mod divertor. These tiles were all unshadowed. Tile dimensions are approximately 2 cm x 2 cm.*

The degree of "self-mitigation" for UFO disruptions is assessed by comparison to intentional MGI mitigation. A set of discharges terminated using predominantly argon MGI are compared with discharges that fit the criteria of a UFO event. The discharges are chosen to have comparable plasma currents and thereby comparable magnetic energies. Although thermal energy may vary between these discharges, it is noted that C-Mod often operated at low beta poloidal where magnetic energy dominates over the thermal energy. The radiated power is measured using a wide-angle (~2π steradians) AXUV diode mounted on the outboard wall of C-Mod. The MGI-terminated discharges show reproducible radiated power time traces with similar absolute magnitude (see Figure 5.2.3 right). In contrast, the UFO disruptions often exhibit lower absolute radiated powers and much larger shot-to-shot variance. Two important experimental uncertainties should be noted. First, this radiated power measurement is sensitive to the location of the radiation that is in view of the detector, and is blind to radiation in half of the torus. Second, AXUV diodes are known to have strong spectral sensitivity [Gray2004], and therefore different temperature evolutions of the dominant radiation zone can lead to different inferred powers. Nevertheless, it can be concluded that the radiation from a UFO event is not reproducible, and either significant localization of the radiation or significant variation in the radiated power occurs. These aspects of UFO disruptions make them distinct from mitigated disruptions, and suggest that first wall melting might still be expected.
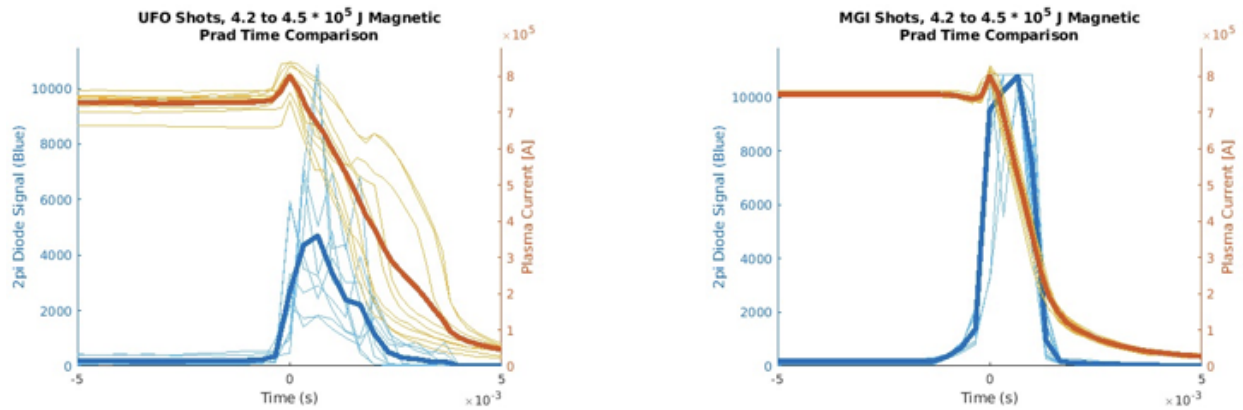
Figure 5.2.3: *(left) Plasma current and radiated power as measured by a wide-angle AXUV diode during UFO disruptions in Alcator C-Mod. (right) Same measurements as (a) but for predominantly argon massive gas injection shutdowns in C-Mod.*

Electromagnetic forces are also a concern for reactors and these forces are a strong function of the current quench temporal evolution. Elongated plasmas often go vertically unstable during the CQ due to strong perturbations introduced during the TQ. When the current quench is long relative to the vertical growth rate, the plasma carries more current off-axis where it drives vertical forces through eddy and halo currents [Clauser2019]. When the current quench is fast relative to the resistive wall time strong eddy currents are driven in first wall components and the vessel [Lehnen2015]. The current quench duration during UFO events in C-Mod varies by a factor of 3x and in some cases exhibits secondary MHD events marked by multiple plasma-current 'spikes' (Figure 5.2.3). This is contrasted by the very reproducible current quench evolution following argon MGI. The MGI shutdowns in C-Mod exhibit a current quench duration comparable to the shortest duration UFO events, but this will be tuned in ITER and future reactors by controlling the quantity of impurity injected.

These results from the C-Mod analysis emphasize the importance of a thorough disruption prediction, avoidance, and mitigation system, for example through real-time monitoring of the first wall for hot spots. This statement applies equally to any DMS technology, and not specifically to SPI.

Recent Publications from DIII-D, JET, and KSTAR SPI Research (FY 2021)

Additional details of recent SPI research, including technology and diagnostic developments, can be found in the following publications, which have been published or submitted during FY 2021. These works are listed here by facility, including those that describe work from multiple machines.

(The full list of general works cited in this report are given separately. See: "References".)

Multi-machine:

L. Baylor, et al., "Design and performance of shattered pellet injection systems for JET and KSTAR disruption mitigation research in support of ITER" 2021 Nucl. Fusion **61** 106001

C. Paz-Soldan, et al., "A Novel Path to Runaway Electron Mitigation via Deuterium Injection and Current-Driven MHD Instability", Nucl. Fusion, Submitted 2021

D. Shiraki, et al. "DIII-D and international research towards extrapolating shattered pellet injection performance to ITER", Preprint: 28th IAEA Fusion Energy Conf. (Nice, France, 10-15 May 2021) [EX/5-2Ra]

DIII-D:

E. Hollmann, et al. "Observation of non-thermal electron formation during the thermal quench of shattered pellet injection shutdowns in DIII-D" 2021 Nucl. Fusion **61** 016023

R. Sweeney, et al. "3D radiation, density, and MHD structures following neon shattered pellet injection into stable DIII-D Super H-mode discharges", 2021 Nucl. Fusion **61** 066040

JET:

S. Jachmich, et al. "Shattered pellet injection experiments at JET in support of the ITER Disruption Mitigation System design", 2021 Nucl. Fusion, Submitted

J. Lovell, et al. "Methods to determine the radiated power in SPI-mitigated disruptions in JET", Rev. Sci. Instr. **92**, 023502 (2021)

C. Reux, et al. "Demonstration of Safe Termination of Megaampere Relativistic Electron Beams in Tokamaks", Phys. Rev. Lett. **126**, 175001 (2021)

U. Sheikh, et al. "Disruption thermal load mitigation with JET SPI", 2021 Nucl. Fusion, Submitted

KSTAR:

J. Kim, et al. "Disruption mitigation by symmetric dual injection of shattered pellets in KSTAR", 28th IAEA Fusion Energy Conference, 10-15 May 2021, EX/5-3Ra

D.-G. Lee, et al., "The new single crystal dispersion interferometer installed on KSTAR and its first measurement", Rev. Sci. Instr. **92**, 033536 (2021)

M.U. Lee, et al. "Radiation measurement in plasma disruption by thin-foil infrared bolometer", Rev. Sci. Instr. **92**, 053536 (2021)

Acknowledgement

Disclaimer

References

[Baylor2015] L.R. Baylor, et al. "Disruption Mitigation System Developments and Design for ITER", Fusion Sci. Tech. **68** (2015) 211

[Baylor2021] L.R. Baylor et al. "Design and performance of shattered pellet injection systems for JET and KSTAR disruption mitigation research in support of ITER", Nucl. Fusion **61** (2021) 106001

[Bandaru2021] V. Bandaru, et al, "Magnetohydrodynamic simulations of runaway electron beam termination in JET", Plasma Phys. Control. Fusion **63** (2021) 035024

[Bonfiglio2020] D. Bonfiglio et al. EFPW 2020

[Clauser2019] C. Clauser, et al., "Vertical forces during vertical displacement events in an ITER plasma and the role of halo currents", Nucl. Fusion **59** (2019) 126037

[Clauser2021] C. Clauser, S. Jardin, R. Raman, B. Lyons, N. Ferraro, "Modeling of carbon pellet disruption mitigation in an NSTX-U plasma", to appear in Nuclear Fusion (2021)

[Combs2010] S. Combs, et al. "Alternative techniques for injection massive quantities of gas for plasma-disruption mitigation", IEEE Trans. Plasma Sci. **38** (2010) 400

[Combs2011] S. Combs, et al. "A technique for producing large dual-layer pellets in support of disruption mitigation experiments", Fusion Sci. Tech. **60** (2011) 473

[Commaux2010] N. Commaux, et al. "Demonstration of rapid shutdown using large shattered deuterium pellet injection in DIII-D", Nucl. Fusion **50** (2010) 112001

[Commaux2011] N. Commaux, et al. "Novel rapid shutdown strategies for runaway electron suppression in DIII-D", Nucl. Fusion **51** (2011) 103001

[Commaux2016] N. Commaux, et al. "First demonstration of rapid shutdown using neon shattered pellet injection for thermal quench mitigation on DIII-D", Nucl. Fusion **56** (2016) 046007

[deVries2016] P.C. de Vries, et al., "Scaling of the MHD perturbation amplitude required to trigger a disruption and predictions for ITER", Nucl. Fusion **56** (2016) 026007

[Gebhart2020] T.E. Gebhart, L.R. Baylor, and S.J. Meitner, "Shatter Thresholds and Fragment Size Distributions of Deuterium-Neon Mixture Cryogenic Pellets for Tokamak Thermal Mitigation", Fusion Sci. Tech. **76** (2020) 831

[Gebhart2021] T.E. Gebhart et al. "Recent progress in shattered pellet injection technology in support of the ITER disruption mitigation system", Nucl. Fusion **61** (2021) 106007

[Gray2004] D. Gray, et al., "Time resolved radiated power during tokamak disruptions and spectral averaging of AXUV photodiode response in DIII-D", Rev. Sci. Instr. **75** (2004) 376

[Herfindal2019] J. Herfindal, et al. "Injection of multiple shattered pellets for disruption mitigation in DIII-D", Nucl. Fusion **59** (2019) 106034

[Hollmann2008] E.M. Hollmann, et al. "Modeling of Fast Radiative Shutdown of Tokamak Discharges Following Massive Gas Injection", Contrib. Plasma Phys. **48** (2008) 260

[Hollmann2015] E.M. Hollmann, et al. "Mitigation of upward and downward vertical displacement event heat loads with upper or lower massive gas injection in DIII-D", Phys. Plasmas **22** (2015) 102506

[Hollmann2019] E.M. Hollmann, et al. "Demonstration of Tokamak Discharge Shutdown with Shell Pellet Payload Impurity Dispersal", Phys. Rev. Lett. **122** (2019) 65001

[Hollmann2020] E.M. Hollmann, et al. "Study of argon expulsion from the post-disruption runaway electron plateau following low-Z massive gas injection in DIII-D", Phys. Plasmas **27** (2020) 042515

[Hollmann2020b] E. Hollmann, et al. "Observation of non-thermal electron formation during the thermal quench of shattered pellet injection shutdowns in DIII-D", Nucl. Fusion **61** (2021) 016023

[Hu2021] D. Hu et al. "Radiation asymmetry and MHD destabilization during the thermal quench after impurity shattered pellet injection", Nucl. Fusion **61** (2021) 026015

[ITER2018] ITER Organization, "ITER Research Plan within the Staged Approach (Level III - Provisional Version)", Report No. ITR-18-003 (2018)

[Izzo2015] V. Izzo et al. "The role of MHD in 3D aspects of massive gas injection", Nucl. Fusion **55** (2015) 073032

[Izzo2021] V.A. Izzo, "Dispersive Shell Pellet Injection Modeling and Validation for DIII-D Disruption Mitigation", Phys. Plasmas, Submitted.

[Jachmich2021] S. Jachmich et al. "Shattered Pellet Injection experiments at JET in support of the ITER Disruption Mitigation System design", Nucl. Fusion, Submitted

[Kim2019] C.C. Kim et al. "Shattered pellet injection simulations with NIMROD", Phys. Plasmas **26** (2019) 042510

[Kim2021] C.C. Kim, et al. "Simulations and Validation of Disruption Mitigation and Projections to ITER's Disruption Mitigation System", Preprint: 28th IAEA Fusion Energy Conf. (Nice, France, 10-15 May 2021) [TH/P3-16]

[Lehnen2015] M. Lehnen, et al. "Disruptions in ITER and strategies for their control and mitigation", J. Nucl. Mater. **463** (2015) 39

[Luce2021] T.C. Luce, et al. "Progress on the ITER DMS Design and Integration", Preprint: 28th IAEA Fusion Energy Conf. (Nice, France, 10-15 May 2021) [TECH/1-4Ra]

[Matsuyama2021] A. Matsuyama, et al. "Requirements for Runaway Electron Avoidance in ITER Disruption Mitigation Scenario by Shattered Pellet Injection", Preprint: 28th IAEA Fusion Energy Conf. (Nice, France, 10-15 May 2021) [TH/P3-12]

[Meitner2017] S. Meitner, et al. "Design and Commissioning of a Three-Barrel Shattered Pellet Injector for DIII-D Disruption Mitigation Studies", Fusion Sci. Tech. **72** (2017) 318

[Parks2017] P.B. Parks, "A Theoretical Model for the Penetration of a Shattered-Pellet Debris Plume", 7th Annual Theory and Simulation of Disruptions Workshop, Princeton, USA (2017)

[Paz-Soldan2019] C. Paz-Soldan, et al. "Kink instabilities of the post-disruption runaway electron beam at low safety factor", Plasma Phys. Control. Fusion **61** (2019) 054001

[Paz-Soldan2021] C. Paz-Soldan, et al. "A novel path to runaway electron mitigation via deuterium injection and current-driven kink instability", Preprint: 28th IAEA Fusion Energy Conf. (Nice, France, 10-15 May 2021) [EX/5-2Rb]

[Raman2019] R. Raman, W. S. Lay, T. R. Jarboe, J. E. Menard, and M. Ono, "Electromagnetic particle injector for fast time response disruption mitigation in tokamaks", Nucl. Fusion **59** (2019) 016020

[Rea2018] C. Rea, et al. "Disruption prediction investigations using Machine Learning tools on DIII-D and Alcator C-Mod", Plasma Phys. Control. Fusion **60** (2018) 084004

[Reux2021] C. Reux, et al. "Demonstration of Safe Termination of Megaampere Relativistic Electron Beams in Tokamaks", Phys. Rev. Lett. **126** (2021) 175001

[Sheikh2021] U. Sheikh, "Disruption thermal load mitigation with JET SPI", Nucl. Fusion, Submitted

[Shiraki2015] D. Shiraki et al. "Characterization of MHD activity and its influence on radiation asymmetries during massive gas injection in DIII-D", Nucl. Fusion **55** (2015) 073029

[Shiraki2016] D. Shiraki et al. "Thermal quench mitigation and current quench control by injection of mixed species shattered pellets in DIII-D", Phys. Plasmas **23** (2016) 062516

[Shiraki2018] D. Shiraki et al. "Dissipation of post-disruption runaway electron plateaus by shattered pellet injection in DIII-D", Nucl. Fusion **58** (2018) 056006

[Shiraki2020] D. Shiraki DIII-D Disruption Mitigation Group Meeting, June 25, 2020

[Shiraki2021] D. Shiraki, et al. "DIII-D and international research towards extrapolating shattered pellet injection performance to ITER", Preprint: 28th IAEA Fusion Energy Conf. (Nice, France, 10-15 May 2021) [EX/5-2Ra]

[Sugihara2007] M. Sugihara, et al. "Disruption scenarios, their mitigation and operation window in ITER", Nucl. Fusion **47** (2007) 337

[Sweeney2020] R. Sweeney et al., "3D Radiation Analysis Following Shattered Pellet Injection in JET and Progress Towards Understanding the Radiation Shortfall", 62nd Annual Meeting of the APS Division of Plasma Physics, Nov. 9-13, 2020, Remote

[Sweeney2021] R. Sweeney et al. "3D radiation, density, and MHD structures following neon shattered pellet injection into stable DIII-D Super H-mode discharges", Nucl. Fusion **61 (**2021) 066040

[Whyte2003] D.G. Whyte, "Disruption mitigation with high-pressure noble gas injection", J. Nucl. Mater. **313** (2003) 1239

52

[Zhu2021] J.X. Zhu, et al. "Hybrid deep-learning architecture for general disruption prediction across multiple tokamaks", Nucl. Fusion **61** (2021) 026007